

RESEARCH ARTICLE

10.1002/2016JE005028

Key Points:

- We developed a full spectral unmixing analysis method to quantitatively study mineral abundances on Mars
- Hydrated minerals including hydrated sulfates, jarosite, and phyllosilicates were identified and analyzed in southwest Melas Chasma, Mars
- The derived abundances provide constraint on the formation processes of hydrated minerals and past aqueous conditions on the study area

Correspondence to:

Y. Liu,
yang.liu@swri.org

Citation:

Liu, Y., T. D. Glotch, N. A. Scudder, M. L. Kraner, T. Conduis, R. E. Arvidson, E. A. Guinness, M. J. Wolff, and M. D. Smith (2016), End-member identification and spectral mixture analysis of CRISM hyperspectral data: A case study on southwest Melas Chasma, Mars, *J. Geophys. Res. Planets*, 121, 2004–2036, doi:10.1002/2016JE005028.

Received 14 MAR 2016

Accepted 2 SEP 2016

Accepted article online 14 SEP 2016

Published online 9 OCT 2016

End-member identification and spectral mixture analysis of CRISM hyperspectral data: A case study on southwest Melas Chasma, Mars

Yang Liu^{1,2}, Timothy D. Glotch¹, Noel A. Scudder^{1,3}, Meredith L. Kraner^{1,4}, Thomas Conduis¹, Raymond E. Arvidson⁵, Edward A. Guinness⁵, Michael J. Wolff⁶, and Michael D. Smith⁷

¹Department of Geosciences, Stony Brook University, Stony Brook, New York, USA, ²Southwest Research Institute, San Antonio, Texas, USA, ³Department of Earth, Atmospheric, and Planetary Sciences, Purdue University, West Lafayette, Indiana, USA, ⁴Nevada Geodetic Laboratory, University of Nevada, Reno, Reno, Nevada, USA, ⁵Department of Earth and Planetary Sciences, Washington University, St. Louis, Missouri, USA, ⁶Space Science Institute, Boulder, Colorado, USA, ⁷NASA Goddard Spaceflight Center, Greenbelt, Maryland, USA

Abstract We present spectral unmixing results over the southwest Melas Chasma region, where a variety of hydrated minerals were identified. We use the Discrete Ordinate Radiative Transfer radiative transfer model to simultaneously model Mars atmospheric gases, aerosols, and surface scattering and retrieve the single-scattering albedos (SSAs) modeled by the Hapke bidirectional scattering function from Compact Reconnaissance Imaging Spectrometer for Mars (CRISM) data. We employ a spectral unmixing algorithm to quantitatively analyze the mineral abundances by modeling the atmospherically corrected CRISM SSAs using a nonnegative least squares linear deconvolution algorithm. To build the spectral library used for spectral unmixing, we use the factor analysis and target transformation technique to recover spectral end-members within the CRISM scenes. We investigate several distinct geologic units, including an interbedded polyhydrated and monohydrated sulfate unit (interbedded unit 1) and an interbedded phyllosilicate-sulfate unit (interbedded unit 2). Our spectral unmixing results indicate that polyhydrated sulfates in the interbedded unit 1 have a much lower abundance (~10%) than that of the surrounding unit (~20%) and thus may have been partially dehydrated into kieserite to form the interbedded strata, supporting a two-staged precipitation-dehydration formation hypothesis. In the interbedded unit 2 phyllosilicates have an abundance of ~40% and are interbedded with ~20% sulfates. The results, in combination with thermodynamic calculations performed previously, suggest that the interbedded phyllosilicates and sulfates likely formed through coupled basalt weathering and evaporation. The methodology developed in this study provides a powerful tool to derive the mineral abundances, aiming to better constrain the formation processes of minerals and past aqueous environment on Mars.

1. Introduction

One important aspect of planetary remote sensing analyses is spectroscopic mineral identification and quantification on the surfaces of the terrestrial bodies. By analyzing the diagnostic features of reflectance spectra in the visible and near-infrared (VNIR; ~0.4–3 μm) region and the thermal emission spectra in the thermal infrared (TIR; ~3–50 μm) region, we can extract valuable mineralogical information. In this case, it is commonly assumed that a pixel (or a spectrum) in a remotely sensed image represents homogeneous characteristics and measures a distinct ground cover mineral. However, the measured signal from the remote sensor always results from the interaction of photons with multiple constituents within each pixel [Keshava and Mustard, 2002]. While multispectral sensing has largely succeeded at classifying whole pixels, image interpretation issues exist as the mixed nature of the spectral information considerably constrains the accuracy of spectral analysis [Adams et al., 1986; Roberts et al., 2004; Keshava and Mustard, 2002; Somers et al., 2011]. With the significant increase of spectral range and resolution in modern hyperspectral data and substantial increases in computing power, we are now in a position to extract and investigate detailed information about the mineral properties of pixels in a remotely sensed scene. This can be done by spectral unmixing, a quantitative analysis procedure that decomposes the measured spectrum of a mixed pixel into a collection of constituent spectra (or end-members) and a set of corresponding fractions (or abundances).

A number of spectral unmixing techniques have been proposed with applications in both terrestrial and extraterrestrial remote sensing studies over the past two decades [e.g., Adams *et al.*, 1986; Johnson *et al.*, 1992; Borel and Gerstl, 1994; Atkinson *et al.*, 1997; Mustard *et al.*, 1998; Carpenter *et al.*, 1999; Guilfoyle *et al.*, 2001; Keshava and Mustard, 2002; Poulet *et al.*, 2002; Li and Mustard, 2003]. Among these techniques, there are generally two categories: linear mixture models and nonlinear mixture models. The linear mixture models assume that single scattering dominates and the albedo of an image pixel is a linear combination of the albedo and the percentage of each end-member, whereas the nonlinear mixture models assume that the multiple scattering dominates and the mixing systematics between these intimate components are highly nonlinear [Keshava and Mustard, 2002]. The linear assumption has shown to be largely valid in the thermal infrared region [Thomas and Salisbury, 1993; Ramsey and Christensen, 1998; Rogers and Aharonson, 2008], because grains have low single-scattering albedo (SSA) values (i.e., high opacity) and it is unlikely that photons can go through multiple grains on the way to the sensor. In VNIR spectral region, however, linear unmixing models do not work well, as the grain optical skin depth approaches the grain size. Thus, nonlinear mixture models have been largely applied in this spectral region due to the complex interactions of several parameters including grain size, abundance, and texture [Nash and Conel, 1974; Singer, 1981; Clark, 1983; Johnson *et al.*, 1992].

Spectral mixture analysis techniques have been extensively applied to the study of the Earth, yet have seen limited use for other planetary bodies, particularly with respect to VNIR data from recent missions. Taking Mars as an example, orbital hyperspectral imaging data from the Observatoire pour la Minéralogie, l'Eau, les Glaces et l'Activité (OMEGA) [Bibring *et al.*, 2004] on board Mars Express and the Compact Reconnaissance Imaging Spectrometer for Mars (CRISM) [Murchie *et al.*, 2007] on board Mars Reconnaissance Orbiter (MRO) have revealed diverse and complex products of aqueous alteration, including hydrated sulfates, phyllosilicates, and hydrated silica [Bibring *et al.*, 2005; Gendrin *et al.*, 2005; Arvidson *et al.*, 2005; Poulet *et al.*, 2005; Mustard *et al.*, 2008; Milliken *et al.*, 2008; Ehlmann *et al.*, 2009; Murchie *et al.*, 2009a]. The discovery of these minerals has advanced our understanding of Martian ancient aqueous history. Although the initial mineral identifications and analyses provided clues to their alteration environments, the mineral assemblages comprising the sediments and the relative abundances of the single minerals can further provide unique constraints to their formation environments. For instance, the abundances in phyllosilicate-bearing rocks on Mars are critical for distinguishing sedimentary rocks that may be thoroughly altered and physically processed from rocks that may be slightly altered with trace amounts of water [Ehlmann *et al.*, 2013]. Quantitative evaluation can thus provide important constraints on how geochemical reservoirs were partitioned between phyllosilicate-bearing rocks and their protoliths [Ehlmann *et al.*, 2013], which can give further information on past aqueous geochemistry and climate conditions on Mars. Therefore, mineral abundance estimates through spectral mixture analysis of orbital hyperspectral data have become necessary to further our understanding of the geologic history of Mars, although retrieving mineral abundances from a reflectance spectrum in an unambiguous way is difficult.

Previous studies have shown the potential utility of quantitative compositional analysis of Martian surface mineralogy. For example, using a nonlinear unmixing model based on the radiative transfer model of Shkuratov *et al.* [1999], Poulet *et al.* [2008, 2009] mapped mineral abundances at Martian phyllosilicate-bearing regions and mafic-rich units using OMEGA and CRISM visible to near-infrared VNIR data. They also calculated the mineral abundances at the final four Mars Science Laboratory (MSL) landing sites with CRISM VNIR data [Poulet *et al.*, 2014]. Poulet *et al.*'s [2008, 2009, 2014] method utilizes a downhill simplex algorithm to invert the spectral data for mineral abundances and grain sizes, optimizing for the lowest RMS error between the measured spectrum and a computed spectrum. Combe *et al.* [2008] performed linear mixture analysis using the Multiple-Endmember Linear Spectral Unmixing Model (MELSUM) on OMEGA data. MELSUM is based on the inversion of linear spectral mixtures using a least squares approach. Recently, Goudge *et al.* [2015] identified and estimated the abundance of halloysite within Kashira crater through nonlinear unmixing utilizing both CRISM-derived and laboratory-derived end-members, demonstrating a promising application of the quantitative analysis of CRISM data. Also, using the mineral abundances and grain sizes derived from Hapke modeling of single-scattering albedos that are retrieved from CRISM data in conjunction with other data sets, Edwards and Ehlmann [2015] investigated the largest exposed carbonate-bearing rock unit on the Nili Fossae plains and evaluated the timing and carbon sequestration potential of rocks on Mars.

In most existing models, the hyperspectral data of OMEGA and CRISM used for spectral mixture analysis have been atmospherically corrected using the empirical volcano scan method [Langevin *et al.*, 2005]. The "volcano

scan" correction attempts to minimize atmospheric gas absorption features by dividing each I/F spectrum (radiance detected by instrument/solar radiance divided by π) by a scaled atmospheric transmission spectrum, in which the scattering effects of atmospheric aerosols are not explicitly corrected. Although *Poulet et al.* [2009] have shown that their modeling method can be confidently used on the OMEGA spectra uncorrected for aerosols, examination of volcano scan corrected reflectance spectra for CRISM data showed undesired atmospheric absorptions and albedo variations as well as higher-than-actual values of corrected I/F at most wavelengths [*Murchie et al.*, 2009b; *Wiseman et al.*, 2014]. Thus, using volcano scan corrected spectra may cause potentially large errors in the spectral mixture analysis of CRISM data.

In this study, we develop and perform complete spectral mixture analysis on CRISM hyperspectral VNIR reflectance data that have been atmospherically corrected for both gases and aerosols using radiative transfer modeling. Although mixing of reflectance spectra in the VNIR region has been shown to be nonlinear [*Nash and Conel*, 1974; *Singer*, 1981; *Clark*, 1983; *Johnson et al.*, 1992], conversion of reflectance data to single-scattering albedos allows for linear unmixing [*Hapke*, 1981]. To do so, we atmospherically corrected CRISM I/F spectra using the Discrete Ordinate Radiative Transfer (DISORT) code [*Stamnes et al.*, 1988] by simultaneously modeling Martian atmospheric gases, aerosols, and surface scattering. Single-scattering albedos were retrieved assuming that surface scattering can be modeled using the Hapke bidirectional scattering function [*Hapke*, 1993]. Because single-scattering albedos add linearly, a library of mineral SSAs (generated using mineral optical constants and assumed mineral grain sizes) was used for linear spectral unmixing of CRISM SSAs. Using this technique, we conducted a case study over Melas Chasma, where hydrated sulfates, jarosite, and phyllosilicates have been identified [*Liu et al.*, 2012a; *Liu and Catalano*, 2016], and derived mineral abundances in the area. We then used the inferred mineral abundances to better constrain their extent, formation mechanisms, and the regional alteration environment.

2. Study Area

We performed spectral unmixing analysis over the southwest Melas Chasma region on Mars. Melas Chasma is the widest segment of the Valles Marineris and is located in the center of the canyon system (Figure 1). It contains extensive and highly organized Hesperian-aged valley networks and alluvial fans [*Mangold et al.*, 2004; *Quantin et al.*, 2005]. Light-toned materials associated with interior layered deposits (ILDs) have been identified within the basin and along the wall rock of Melas Chasma [*Weitz et al.*, 2003; *Weitz et al.*, 2015]. Also, evidence for thin-skinned deformation of sedimentary rocks has been observed in Melas Chasma and is interpreted to have been produced by a slow subaerial or subaqueous landslide and liquefaction [*Metz et al.*, 2010]. CRISM multiple survey parameter (MSP) maps indicate that southwest Melas Chasma contains widespread hydrated minerals (Figure 1). Furthermore, high spatial and spectral resolution orbital VNIR spectroscopy of Mars using OMEGA and CRISM data has also revealed a variety of hydrated minerals that form from aqueous alteration, including hydrated sulfates and phyllosilicates [*Gendrin et al.*, 2005; *Weitz et al.*, 2015; *Liu et al.*, 2012a; *Liu and Catalano*, 2016].

Specifically, in the southern wall and nearby floor of Melas Chasma, a sequence of interbedded polyhydrated and monohydrated sulfate deposits were identified within the ILDs using CRISM hyperspectral data [*Liu et al.*, 2012a]. The interbedded sulfate layers were interpreted to have formed by cyclic deposition of the two hydrated sulfate phases from two episodic brines with different chemistries or repeated deposition of polyhydrated sulfates and partial dehydration of polyhydrated sulfates into monohydrated sulfates. The jarosite-bearing units were also identified stratigraphically above the hydrated sulfate deposits and thus postdate the lower Mg sulfate units. These were hypothesized to have formed either by oxidation of a fluid containing Fe(II) and SO_4 or by leaching of soluble phases from precursor intermixed jarosite-Mg sulfate units that may have formed during the later stages of deposition of the hydrated sulfate sequence.

To the west of the interbedded sulfates layers, we identified and mapped a sequence of interbedded Fe/Mg smectite and hydrated sulfate deposits [*Liu and Catalano*, 2016]. *Liu and Catalano* [2016] performed equilibrium thermodynamic calculations of coupled basalt weathering and fluid evaporation, and the results predict that sequential formation of smectites and sulfate evaporites, as observed in the interbedded smectite-sulfate sequence, is chemically plausible. The smectite-sulfate deposits were thus interpreted to have formed through in situ basalt weathering and fluid evaporation, although an origin of transport and deposition of

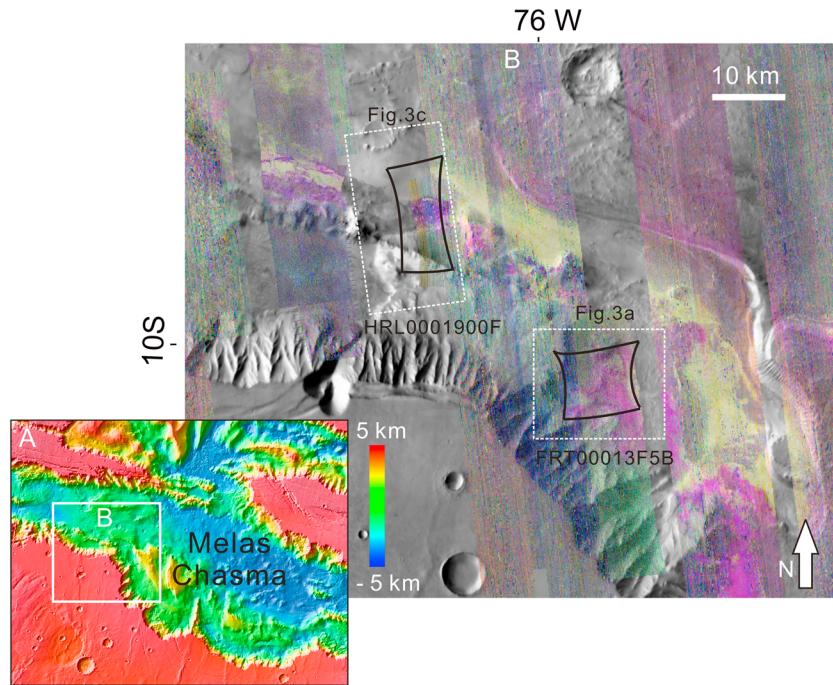


Figure 1. Southwest Melas Chasma. (a) Regional context. The hill shaded map is produced from MOLA topographic data, and southwest Melas Chasma is indicated by white box. (b) CRISM multiple survey (MSP) index maps (R = SINDEX, G = BD2100, and B = BD1900) [Viviano-Beck *et al.*, 2014] overlaid on Thermal Emission Imaging System daytime mosaic. CRISM MSP data have ~200 m/pixel spatial sampling and 72 selected bands and are used for global mapping mineralogy. Red represents polyhydrated sulfates, and yellow represents monohydrated sulfates.

detrital phyllosilicates by a neutral fluid containing Mg and SO_4 and subsequent evaporation cannot be entirely ruled out.

The discovery of these hydrated mineral deposits revealed complex ancient aqueous environmental conditions in Melas Chasma. Although these initial mineral identifications provided clues for their alteration environments, the mineral assemblage comprising the deposits and the relative abundances of the single minerals can further provide unique constraints on their formation environments. Thus, this study aims to quantitatively map the abundance of hydrated minerals in southwest Melas Chasma.

3. Data Sets and Methods

3.1. Data Sets

The primary data used for spectral unmixing analysis in this work are hyperspectral image cubes from the CRISM instrument. CRISM has 544 channels covering 0.36–3.92 μm and has a spatial resolution of either full spatial resolution (FRT; 18 m/pixel) or 2 times spatially binned (HRL/HRS; 36 m/pixel) in targeted mode. CRISM data were processed to I/F (spectral radiance detected by the instrument divided by solar spectral irradiance divided by π) by the CRISM science operation center as described by Murchie *et al.* [2007] and can be downloaded from the Planetary Data System. CRISM I/F data were photometrically and atmospherically corrected using radiative transfer modeling for a chosen surface scattering model.

3.2. Surface Scattering Model

The primary scattering models used by planetary scientists to analyze spectra of Mars and other solar system objects are the Hapke's treatment of radiative transfer [e.g., Hapke, 1981; Hapke and Wells, 1981; Hapke, 1993] and the geometric optics model of Shkuratov [Shkuratov *et al.*, 1999]. Both the Hapke and Shkuratov models have been used to retrieve mineral abundances from VNIR spectra of the Moon [e.g., Cahill *et al.*, 2009], asteroids [e.g., Clark, 1995; Clark *et al.*, 2001; Poulet *et al.*, 2002], and well-characterized laboratory standards [e.g., Hiroi and Pieters, 1994; Poulet and Erard, 2004; Lawrence and Lucey, 2007; Denevi *et al.*, 2008; Lucey and

Noble, 2008]. In this study, we use a Hapke-based radiative transfer model to simulate Mars surface scattering properties. Hapke's model is a more rigorous treatment of scattering on planetary surfaces. Shkuratov model does not account for the phase geometry, and the refractive indices used in the model are not independent of grain size. Hapke's model allows for the possibility that composite materials can be treated as a mixture of bidirectional reflectance distribution function models through a weighted combination of the single-scattering albedos of the individual components [*Hapke and Wells, 1981; Clark, 1983; Clark and Roush, 1984; Mustard and Pieters, 1989*], which enables us to perform linear mixture analysis of the observed spectra.

The Hapke bidirectional reflectance function is described as the following equation [*Hapke, 1993*]:

$$rf(i, e, g) = \frac{w}{4} \frac{\mu_0}{\mu_0 + \mu} \{ [1 + B(g)]p(g) + H(\mu_0)H(\mu) - 1 \} S(i, e, g) \quad (1)$$

where $rf(i, e, g)$ is the radiance factor, equivalent to CRISM I/F; i, e , and g are incidence, emergence, and phase angles, respectively; μ_0 is the cosine of the incidence angle, and μ is the cosine of the emergence angle; w is the average single particle scattering albedo defined as the ratio of scattering efficiency to the sum of scattering and absorption efficiencies and is the primary scattering parameter to be retrieved; $p(g)$ is the surface phase function describing the angular distribution of light intensity scattered by a single particle; $B(g)$ is the opposition effect describing the sharp surge in brightness around the zero phase angle; H is the multiple scattering function; and S is the shadowing function defined by a macroscopic roughness parameter, $\bar{\theta}$. The surface phase function is modeled as a two-term Henyey-Greenstein function, which is dependent on the phase angle and one asymmetry parameter:

$$p(g) = \frac{1+c}{2} \frac{(1-b^2)}{(1-2bc\cos(g)+b^2)^{3/2}} + \frac{1-c}{2} \frac{(1-b^2)f}{(1+2bc\cos(g)+b^2)^{3/2}} \quad (2)$$

where b (asymmetry factor) is the angular width of the scattering lobes and ranges from 0 to 1 in value; c (forward scattering fraction) describes the magnitude of the backscatter lobe (first term) relative to the forward-scatter lobe (second term) and ranges from -1 to 1 in value. Negative c values describe a more backscattering surface, $c=0$ describes isotropic scattering, and positive c values describes a forward scattering surface. The opposition effect is defined by

$$B(g) = \frac{B_0}{1 + (1/h)\tan(g/2)} \quad (3)$$

where $B(g)$ is the amplitude and h is the angular width. The H function is approximated by

$$H(x) = \frac{1+2x}{1+2\sqrt{1-wx}} \quad (4)$$

where x is either μ_0 or μ , and $\sqrt{1-w}$ is the albedo factor.

3.3. Single-Scattering Albedo Retrieval From CRISM Hyperspectral Data

The CRISM I/F spectra at the top of the Martian atmosphere include radiative contributions from both the atmosphere and the surface. To remove the atmospheric contributions caused by the absorption, scattering, and emission of gas and aerosols and to retrieve the surface single-scattering albedos, we use the Discrete Ordinate Radiative Transfer (DISORT) modeling approach developed by *Stamnes et al. [1988]*. As implemented in a FORTRAN numerical code, the DISORT radiative transfer model applies to the inhomogeneous plane-parallel atmosphere with vertical discretization of atmospheric properties. The surface with either Lambertian or non-Lambertian reflection properties can be treated as the lower boundary of the atmospheric layers. DISORT can simulate the atmospheric and surface contributions to the radiance and calculate the modeled I/F on the detector.

In this study, to simulate CRISM I/F spectra we first use the Hapke bidirectional reflectance function [*Hapke, 1993*] to model the surface scattering properties at the lower boundary within the DISORT. The description of the scattering parameters in the Hapke model is detailed in section 3.2. Based on the previous studies by *Wolff et al. [2009]*, we used an asymmetry parameter b of 0.3, forward scattering fraction c of 0.6, opposition surge amplitude B_0 of 1.0, width of opposition surge h of 0.06, and roughness parameter $\bar{\theta}$ of 15.0. To model the Martian atmospheric contributions to the CRISM I/F, several input parameters are required for

DISORT calculations. These parameters include dust and ice aerosol optical depth, wavelength-dependent dust particle single-scattering albedo and phase function, CO₂ and CO concentrations, water vapor abundances, surface pressure, and atmospheric temperature and pressure profiles. Descriptions of the derivation of these parameters have been detailed in previous work [Arvidson *et al.*, 2006; Wolff *et al.*, 2007, 2009; Cull *et al.*, 2010a; Cull *et al.*, 2010b; Liu *et al.*, 2012b; Shaw *et al.*, 2013; Wiseman *et al.*, 2014]. The viewing geometry derived from CRISM-Derived Data Records including incidence, emergence, and phase angles is also required for modeling the surface scattering and the atmosphere.

For each CRISM channel, model I/F values are calculated for a given single-scattering albedo and the atmospheric conditions when the CRISM observation was taken. A lookup table approach was used to retrieve the single-scattering albedos from the observed CRISM I/F. CRISM is affected by the “spectral smile” and also has a small temperature dependent wavelength shift, which can cause errors in the 2 μm wavelength region. To mitigate the inaccuracies in wavelength calibration, we use a table of wavelength offsets calculated for each CRISM observation [Smith *et al.*, 2009]. Also, in our modeling, spectrally flat regions dominated by basalt sands in the scene were used to help pin down the right pressures such that the retrieved single-scattering albedos in these regions do not have any dips or bumps in the 2 μm wavelength region. In the regions with hydrated phase signatures, the pressure scale height was then adjusted with the Mars Orbiter Laser Altimeter (MOLA)-based elevations within the scene to minimize the residue of CO₂ gas absorptions in the retrieved single-scattering albedos.

3.4. Recovery of CRISM Spectral End-Members

After CRISM single-scattering albedos were retrieved, they were recast into radiance coefficients using the same lighting and viewing geometry under which laboratory spectra are acquired. The radiance coefficient data are then used for the recovery of spectral end-members. One way to achieve this is to compare the retrieved CRISM radiance coefficient spectra with laboratory spectra, as each mineral has diagnostic absorption features that provide a unique “fingerprint” of the mineral. By comparison with reference spectral library spectra, this fingerprint allows for identification of the material.

To identify spectral end-members, we also use factor analysis and target transformation (FATT) [Malinowski, 1991], a statistical principal component-based approach. This method has been primarily applied to mid-IR remote sensing data sets [Bandfield *et al.*, 2000; Glotch *et al.*, 2006; Glotch and Rogers, 2013] but has recently been successfully applied to VNIR remote sensing data sets from Mars and the Moon [Thomas and Bandfield, 2013; Che and Glotch, 2014; Friedlander *et al.*, 2015]. Factor analysis can be applied to any data set with independently varying components that add linearly. Since single-scattering albedos of minerals in VNIR combine linearly for given grain sizes and packing, the FATT algorithm can be used to identify end-members from a spectral image cube based on the uniqueness of each end-member.

Factor analysis transforms the CRISM spectra of interest into two abstract row and column matrices (i.e., eigenvector matrices) with associated eigenvalues, which indicate their relative importance. Typically, less than 10 eigenvectors are needed to fully reproduce the spectral variation in a scene within the level of noise.

The derived eigenvectors represent meaningful variability within a data set. To relate the eigenvectors back to mineral spectra in the scene, the eigenvectors must be transformed into physically meaningful components using target transformation. Target transformation rotates the coordinate axes of the abstract matrices and aligns them in a fashion that yields a physically meaningful vector. To do this, we perform a linear least squares fit [e.g., Ramsey and Christensen, 1998] of the eigenvectors onto a test spectrum (typically taken from the CRISM or Reflectance Experiment Laboratory (RELAB) spectral libraries, or acquired in house at the Stony Brook Vibrational Spectroscopy Laboratory) that is thought to be a component of the system. If the best fit spectrum is an acceptable match to the test spectrum, then it is likely a component in the data being analyzed. Additional details on the FATT process can be found in Malinowski [1991], Bandfield *et al.* [2000], and Glotch *et al.* [2006].

3.5. Spectral Unmixing of Retrieved CRISM Single-Scattering Albedos

The fundamental goal of spectral mixture analysis is to fit an observed spectrum with a suite of spectral end-members using the least squares technique, subject to the constraint that the sum of the weighted fractions is unity [Adams *et al.*, 1993]. Depending on the scattering models used, the spectral end-members can either be taken directly from laboratory measurements or indirectly computed from measured scene spectra. The

spectral end-member library of single-scattering albedos used in this study is one that cannot be directly measured. The single-scattering albedo is dependent on grain size and the optical constants (the real and imaginary indices of refraction n and k), which define a mineral's optical properties. To make the spectral library of the single-scattering albedos, mineral optical constants were first obtained using the Shkuratov radiative transfer model [Shkuratov *et al.*, 1999; Martone and Glotch, 2014] or the Hapke radiative transfer model [Sklute *et al.*, 2015]. Single-scattering albedos were then calculated based on the Hapke model for a given grain size using the following equation:

$$w = S_e + (1 - S_e) \frac{(1 - S_i)\Theta}{1 - S_i\Theta} \quad (5)$$

where S_e is the reflectivity for the external incident light and is a function of both n and k :

$$S_e = \frac{(n - 1)^2 + k^2}{(n + 1)^2 + k^2} + 0.05 \quad (6)$$

and S_i is the reflectivity for the internal incident light and is expressed as

$$S_i = 1.014 - \frac{4}{n(n + 1)^2} \quad (7)$$

Θ is the particle internal transmission coefficient and is defined as

$$\Theta = \frac{r_i + e^{-\sqrt{\alpha(a+s)D}}}{1 + r_i e^{-\sqrt{\alpha(a+s)D}}} \quad (8)$$

where r_i is the internal diffuse reflectance inside the particle, D is the particle diameter (grain size), and s denotes the internal volume scattering coefficient. r_i is defined as

$$r_i = \frac{1 - \sqrt{\alpha/(a+s)}}{1 + \sqrt{\alpha/(a+s)}} \quad (9)$$

where α is the absorption coefficient for the internal attenuation, defined as

$$\alpha = \frac{4\pi k}{\lambda} \quad (10)$$

Hapke and Wells [1981] found the value of s parameter to be 600 cm^{-1} for ground silicate glass, although they could not explain why such a large value was required, whereas Lucey [1998] found that a value of 0 gives an adequate fit to the data from particulate mineral samples. In this study we set the value of s as 0 which implies no internal scattering.

Single-scattering albedos of individual components can add linearly to model the mixed SSAs for the whole assemblage using the following equation

$$w_{\text{mix}} = \sum_i \frac{M_i \omega_i}{\rho_i D_i} / \sum_i \frac{M_i}{\rho_i D_i} \quad (11)$$

[Hapke, 1981], where M_i is the mass fraction, ρ_i is the density, D_i is the average effective particle size, and ω_i is the single-scattering albedo for the i th end-member. To perform the spectral unmixing, the atmospherically corrected CRISM single-scattering albedos were modeled using a nonnegative least squares (NNLS) linear deconvolution algorithm [Rogers and Aharonson, 2008] through the open source software package DaVinci, which is maintained by the Mars Space Flight Facility at Arizona State University (<http://davinci.asu.edu>) in partnership with other institutions. For each CRISM single-scattering albedo spectrum, the model must reproduce the shape and depth of each of the absorption bands, the spectral continuum, and the absolute value of the reflectance. The script runs the model over all possible combinations of spectral end-member single-scattering albedos and selected grain sizes, not only excluding unwanted end-members and grain sizes but also allowing for mineral-specific grain size inclusions. The total number of combinations can be calculated by C_r^n where n is the total number of grain sizes in the library and r is the number of grain sizes per run in our iteration calculations. For example, 20 grain sizes in the grain size library and 5 grain sizes per run give a total number of 15504 (i.e., C_5^{20}) combinations. The selection of end-members for each

Table 1. Spectral Library End-Members Used for Spectral Unmixing Model

Mineral Class	Mineral	Chemical Formula
Primary minerals	Anorthite (plagioclase)	CaAl ₂ Si ₂ O ₈
	Augite (high-calcium pyroxene)	(Ca,Na)(Mg,Fe,Al,Ti)(Si,Al) ₂ O ₆
	Forsterite (Mg-olivine)	Mg ₂ SiO ₄
	Labradorite (plagioclase)	(Ca,Na)(Si,Al) ₄ O ₈
	Diopside (high-calcium pyroxene)	CaMgSi ₂ O ₆
	Enstatite (low-calcium pyroxene)	Mg ₂ Si ₂ O ₆
Silicates	Celadonite	K(Mg,Fe ²⁺)(Fe ³⁺ ,Al)(Si ₄ O ₁₀)(OH) ₂
	Kaolinite	Al ₂ Si ₂ O ₅ (OH) ₄
	Montmorillonite	(Na,Ca) _{0.33} (Al,Mg) ₂ (Si ₄ O ₁₀)(OH)
	Vermiculite	(Mg,Fe ²⁺ ,Al) ₃ (Al,Si) ₄ O ₁₀ (OH) ₂ •4(H ₂ O)
	Nontronite	Na _{0.3} Fe ³⁺ Si ₃ AlO ₁₀ (OH) ₂ •4(H ₂ O)
	Saponite	Ca _{0.1} Na _{0.1} Mg _{2.25} Fe _{0.75} Si ₃ AlO ₁₀ (OH) ₂ •4(H ₂ O)
	Amorphous opaline silica	SiO ₂ •n(H ₂ O)
Sulfates	Kieserite	MgSO ₄ •H ₂ O
	Epsomite	MgSO ₄ •7H ₂ O
	Rozenite	FeSO ₄ •4H ₂ O
	K-jarosite	KFe ³⁺ (SO ₄) ₂ (OH) ₆
	Carbonate	Ankerite
Calcite		CaCO ₃
Dolomite		CaMg(CO ₃) ₂
Magnesite		MgCO ₃
Siderite		FeCO ₃
Oxides/hydroxides		Ferrihydrite
	Goethite	FeO(OH)
	Schwertmannite	Fe ³⁺ ₁₆ O ₁₆ (OH) ₁₂ (SO ₄) ₂
Halides	Halite	NaCl
Other	Mars dust	Unknown composition

unmixing model was based on FATT modeling and visual inspection. Note that the grain size is not a free parameter in our model. This method has one advantage over the downhill simplex minimization method because more control over the process of minimization is exerted by avoiding unrealistic grain sizes for certain phases, which gives more reliable results. Spectra were modeled through several iterations to produce the best mathematical and visual fit by optimizing for the lowest RMS error between the retrieved and the modeled single-scattering albedos, providing mineral abundances and grain sizes for each spectrum.

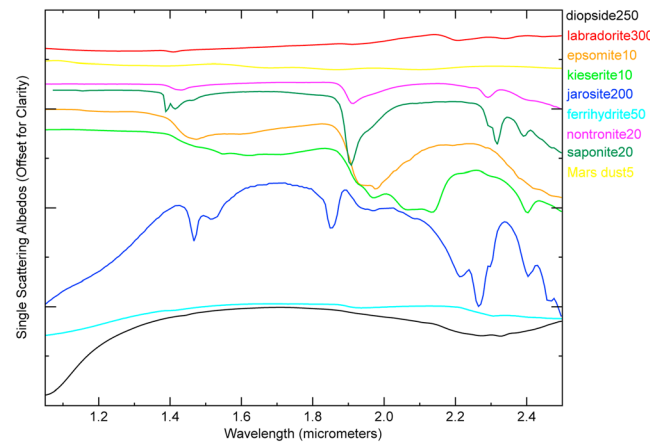


Figure 2. Example of synthesized single-scattering albedo spectra that are used as spectral end-members in our modeling. Grain sizes are indicated after mineral names on the right of the plots.

3.6. End-Member Selection for Spectral Unmixing

The selection of minerals as end-members to be included in the unmixing modeling is critical. A wide variety of minerals, including primary unaltered silicates, secondary chemical weathered silicates (e.g., phyllosilicates), hydrated sulfates, carbonates, and oxides and hydroxides, have been selected to build the single-scattering albedo spectral library. The list of these minerals with their chemical formulas is shown in Table 1. Carbonate and some common phyllosilicates that are identified on Mars were included, although most of them have been excluded in our unmixing model based on the FATT

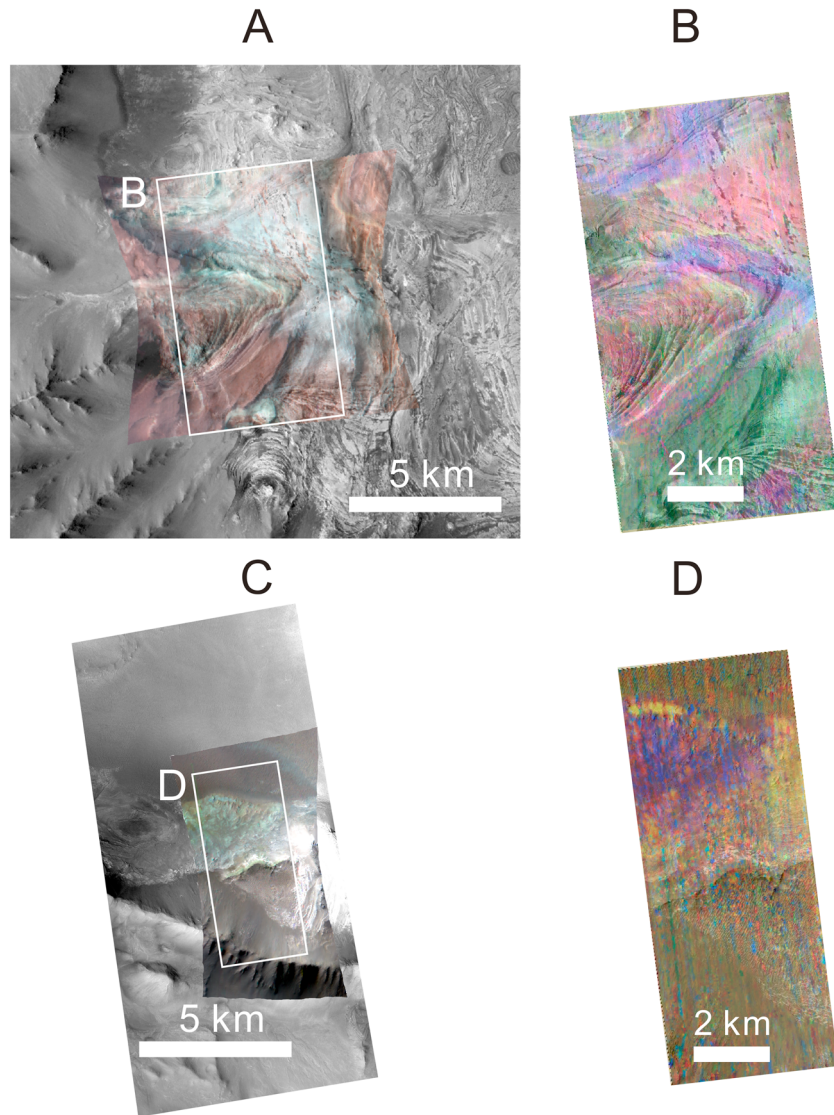


Figure 3. (a) CRISM false color image for FRT00013F5B superimposed on the CTX imagery (B11_014062_1697). (b) CRISM FRT00013F5B hyperspectral index map (R = SINDEXT, G = BD2100, B = BD2265) [Viviano-Beck *et al.*, 2014] superimposed on the HiRISE imagery (EPS_014062_1695). (c) CRISM false color image for HRL0001900F superimposed on the CTX imagery (B21_017952_1701). (d) CRISM HRL0001900F index map (R = SINDEXT, G = BD2100, B = BD2290) [Viviano-Beck *et al.*, 2014] superimposed on the HiRISE imagery (ESP_017952_1700).

modeling results and visual inspection of CRISM spectra of the sites analyzed. Primary minerals such as plagioclase, pyroxene, and olivine are included in the spectral library. Although Fe-free plagioclase is featureless, the presence of such a mineral in the library accounts for the reduced spectral contrast for the H₂O, OH, and metal-OH bands in the CRISM spectra as compared to the pure library spectra [Poulet *et al.*, 2008]. Martian dust is also added to the spectral end-member library, although the composition of this complex mixture is poorly known and needs to be thoroughly addressed in future studies. In this work, we use the complex indices of refraction derived by Wolff *et al.* [2009] with CRISM emission phase function sequences to model dust single-scattering albedos, and the dust was treated as a single material and was normalized out when calculating mineral abundances. An example of selected single-scattering albedos at given grain sizes from our spectral library is shown in Figure 2. To convert mineral optical constants into single-scattering albedos to be used in our model, we assign several possible grain sizes to each mineral and create an end-member library consisting of multiple single-scattering albedos for each mineral. Additionally, synthetic positive and negative slope end-members

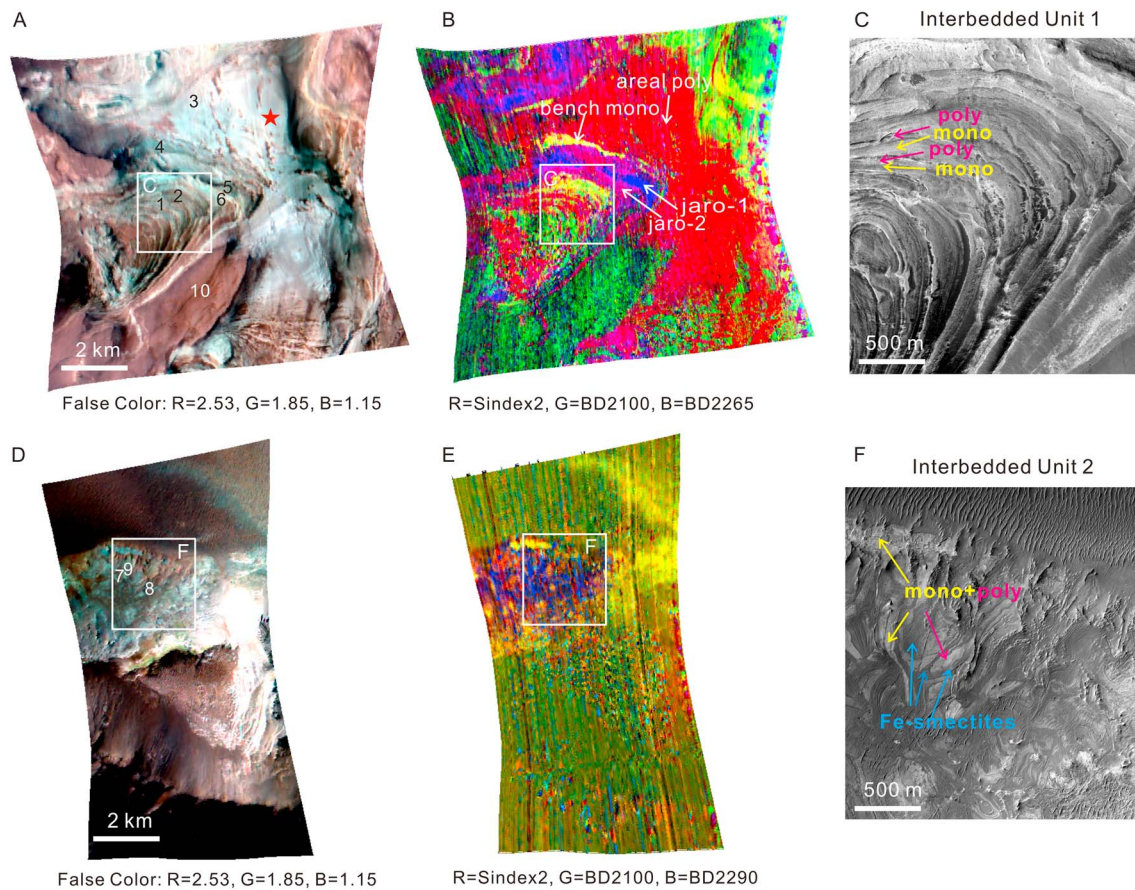


Figure 4. (a) CRISM false color image for FRT00013F5B. Numbers 1–6 indicate the location where the spectra were extracted for spectral unmixing model. (b) CRISM index map for FRT00013F5B. Stretches were applied for R, G, and B bands as 0–0.026, 0–0.01, and 0–0.016, respectively. Red represents polyhydrated-sulfate-rich area, yellow represents monohydrate sulfate rich area, blue represents jarosite rich area (jaro-1 = jarosite-bearing unit 1), and purple represents area with both enhanced 2.265 μm jarosite band and 1.9 water band (jaro-2 = jarosite-bearing unit 2). The interbedded polyhydrated and monohydrated sulfate unit in the interior layered deposits (ILDs) is outlined by white box. Areal polyhydrated sulfates (areal poly, poly = polyhydrated sulfates) and monohydrated sulfates on a bench unit (bench mono, mono = monohydrated sulfates) are also indicated by white arrows. (c) HiRISE subset image of the outlined areas in A and B shows a close look of the interbedded polyhydrated and monohydrated sulfate unit (interbedded unit 1). (d) CRISM false color image for FRT0001900F. Numbers 7–9 indicate the locations where the spectra were extracted for spectral unmixing modeling. (e) CRISM index map for FRT0001900F. Stretches were applied for R, G, and B bands as 0–0.046, 0–0.062, and 0–0.03, respectively. Red represents polyhydrated-sulfate-rich area, yellow represents monohydrate sulfate-rich area, and blue represents clay-rich area. The color variations are not as distinct as that in FRT00013F5B due to the noisier data in HRL0001900F. (f) HiRISE subset image of the outlined areas in D and E shows a close look of the highly deformed interbedded Fe-smectite and hydrated sulfate unit (interbedded unit 2).

were added to account for any differences in spectral slope between the CRISM and laboratory spectra [Poulet *et al.*, 2009].

4. Results

We focus on spectral analysis of two CRISM images (FRT00013F5B and HRL0001900F), where two distinct geological features have been identified previously [Liu *et al.*, 2012a; Liu and Glotch, 2014; Liu and Catalano, 2016]: the interbedded polyhydrated and monohydrated sulfate units and the interbedded phyllosilicates and hydrated sulfate units. A more detailed regional context of the study area is shown in Figure 3, where CRISM false color images are overlain on regional Context Camera (CTX) imagery. Additionally, false color images of the two CRISM scenes together with their parameter maps are shown in Figure 4. The parameter maps were generated from the revised CRISM parameters and summary products of Viviano-Beck *et al.* [2014], where the enhanced colors at SINDEXT2, BD2265, and BD2290 indicate the presence of hydrated sulfates, jarosite, and Fe-phyllosilicates, respectively, in the study area (Figures 4b and 4e). The areas with interbedded polyhydrated and monohydrated sulfate unit (interbedded unit 1) and the interbedded

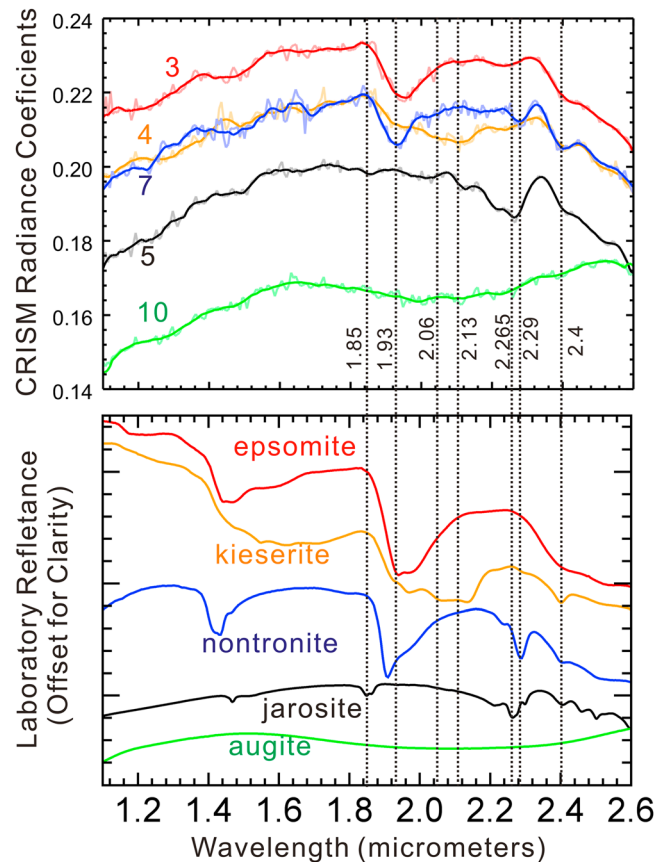


Figure 5. Mineral identification. Comparison between DISORT-retrieved radiance coefficients from CRISM data and laboratory spectra. The number IDs of the CRISM spectra correspond to the numbers indicating the locations of the spectra taken in Figures 4a and 4d. The laboratory spectra are from RELAB at Brown University and were measured at 30 incident angle and 0 emission angle.

(2) spectral unmixing analysis results for individual spectra that were extracted from the regions of interest, and (3) mineral abundance maps for the two CRISM images.

4.1. End-Member Identification

4.1.1. Comparing With Laboratory Spectra

A comparison between the representative retrieved CRISM radiance coefficients over the study area and selected laboratory spectra is shown in Figure 5. A variety of hydrated minerals have been identified in southwest Melas Chasma, including polyhydrated sulfates, kieserite, jarosite, and Fe/Mg smectites. Polyhydrated sulfates are identified by the water absorption feature at $\sim 1.9\ \mu\text{m}$ and a reflectance drop at $2.4\ \mu\text{m}$ due to overtones of the fundamental stretching modes of SO_4 groups associated with H_2O or OH [Cloutis *et al.*, 2006]. Monohydrated sulfates (i.e., kieserite) are identified by the doublet absorption bands at 2.06 and $2.13\ \mu\text{m}$. Jarosite is identified by the absorption band at $1.85\ \mu\text{m}$ due to the overtone of OH bending associated with the SO_4 group and a unique absorption band at $2.265\ \mu\text{m}$. Fe/Mg smectites are identified by the absorption features at 2.29 – $2.31\ \mu\text{m}$ due to metal-OH vibrations. For example, Fe-rich nontronite has an absorption band at $\sim 2.29\ \mu\text{m}$, whereas Mg-rich saponite has an absorption band at $2.231\ \mu\text{m}$. The 2.29 – $2.3\ \mu\text{m}$ absorption band in the CRISM spectra indicates the presence of more iron-rich smectite in our study area. In addition to the hydrated minerals, pyroxenes are identified based on the broad absorption bands around 1 and $2\ \mu\text{m}$ due to crystal field transitions of Fe^{2+} in octahedral sites. Specifically, the band center at $\sim 2\ \mu\text{m}$ in the pyroxene spectra occurs near $2.3\ \mu\text{m}$, indicating the presence of high-calcium pyroxene.

phyllosilicate and hydrated sulfate unit (interbedded unit 2) are outlined with the white boxes, and the morphology of these features is shown in the High-Resolution Imaging Science Experiment (HiRISE) subset images in Figures 4c and 4f. To view the relationship between the interbedded units and the composition better, the CRISM parameter maps have also been superimposed on the HiRISE image and are shown in Figures 3b and 3d. As discussed in our previous studies [Liu *et al.*, 2012a], the interior layered deposits (ILDs) shown in Figure 4c contain alternating layers of relatively bright polyhydrated sulfates and dark monohydrated sulfates. Also, highly deformed folded strata shown in Figure 4f contain relatively bright hydrated sulfates and dark phyllosilicates [Liu and Catalano, 2016]. These previous studies have considered the possible formation mechanisms of these units based on detailed spectral and morphological studies. In this study, we show that quantitative compositional analysis of the spectra extracted from these interbedded units can further constrain their formation mechanisms and thus the aqueous history. In this section, we will present (1) the end-member identification results that were used to construct the spectral libraries for spectral unmixing analysis,

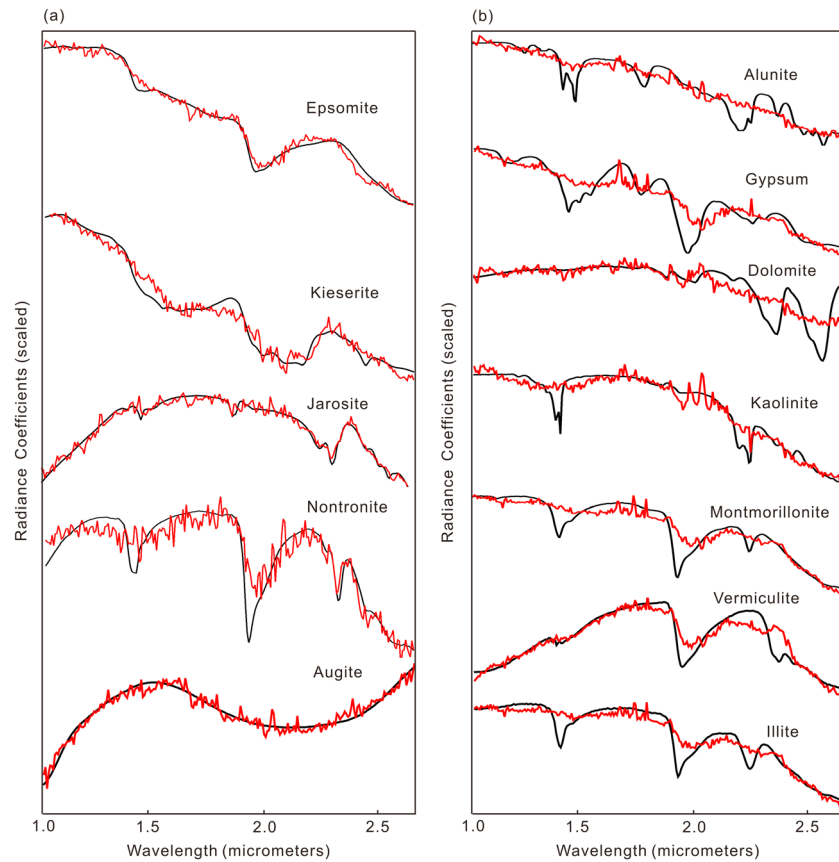


Figure 6. FATT modeling results for both (a) present phases and (b) absent phases in the study areas. The laboratory spectra are in black, and the model spectra are in red.

4.1.2. FATT Analysis Results

The modeled spectra derived from FATT analysis of CRISM reflectance data together with laboratory spectra are shown in Figure 6. Using the CRISM spectral library, we included a variety of hydrated mineral phases in the target transformation library. The model spectra derived from CRISM data are in good agreement with both the positions and shapes of spectral absorption features and spectral slopes of hydrated phases identified by comparing with laboratory spectra (Figure 6a). In addition to hydrated minerals, we also achieved good fits for high-calcium pyroxene such as augite. More importantly, a clear test can be made for the absence of related phases, which enables us to narrow the range of phases used in the spectral mixture analysis. An example of the spectral models for some absent phases determined by the target transformation approach is shown in Figure 6b. Alunite, gypsum, dolomite, kaolinite, montmorillonite, vermiculite, and illite could not be reproduced using the CRISM-derived eigenvectors, indicating their likely absence in the CRISM scene. The FATT technique provides tight constraints on the presence or absence of minor phases and, thus, aids in assembling a library of spectral end-members for each atmospherically corrected CRISM image used for spectral mixture analysis.

4.2. Spectral Unmixing Results

The end-member identification results indicate that southwest Melas Chasma hosts a variety of hydrated materials including polyhydrated and monohydrated sulfates, jarosite, and phyllosilicates. We have modeled CRISM spectra representative of several outcrops with hydrated mineral signatures, to extract the abundances and grain sizes of both hydrous and anhydrous phases. The spectra that we modeled were all averages of 10×10 pixel areas to enhance the signal-to-noise ratio. The locations of the spectra that we extracted to perform spectral unmixing analysis are shown in Figures 4a and 4d, labeled as numbers 1–9. The model abundances, derived grain sizes, RMS errors of the model, and the coordinates of the center pixel for each spot are summarized in Table 2. In general, the primary phases such as plagioclase and pyroxene are

Table 2. Location of the Deposits Examined and the Derived Minerals Abundances and Grain Sizes^a

Spot	Location ^b	Plag		Dust		Pyro		Ferr		Schw		Eps		Kies		Jaro		Nont		Opal		RMS
		V ^c	G ^d	V	G	V	G	V	G	V	G	V	G	V	G	V	G	V	G	V	G	
#1	10.23, 75.49	39	350	28	5	12	75	5	20	-	-	13	5	-	-	2	220	-	-	1	140	0.0025
#2	10.23, 75.48	38	100	36	5	7	75	5	30	-	-	-	-	11	5	3	260	-	-	-	-	0.0032
#3	10.18, 75.47	47	350	12	5	6	100	8	10	-	-	21	5	-	-	2	120	-	-	4	140	0.0024
#4	10.20, 75.49	41	160	23	5	5	180	13	30	-	-	-	-	14	5	4	260	-	-	-	-	0.0028
#5	10.22, 75.45	19	160	36	5	5	180	28	30	-	-	-	-	-	-	12	200	-	-	-	-	0.0029
#6	10.23, 75.46	15	160	26	5	-	-	14	20	34	5	7	5	-	-	5	250	-	-	-	-	0.0025
#7	9.62, 76.01	25	180	14	5	11	200	-	-	-	-	-	-	6	10	-	-	39	5	-	-	0.0028
#8	9.62, 76.00	35	420	9	5	2	200	25	25	-	-	19	5	10	10	-	-	-	-	-	-	0.0027
#9	9.65, 75.99	42	320	-	-	12	200	21	30	-	-	-	-	25	10	-	-	-	-	-	-	0.0024

^aThe abbreviated names of minerals are Plag, Plagioclase; Dust, Mars Dust; Pyro, Pyroxene; Ferr, Ferrihydrite; Schw, schwertmannite; Eps, epsomite; Kies, kieserite; Jaro, jarosite; Nont, nontronite; and Opal, Opal silica.

^bLocation is in the form of coordinates (latitude, eastern longitude) in degrees.

^cV represents volumetric abundance in unit percentage.

^dG represents grain size in microns.

mostly present for each spot. Plagioclase has relatively larger volume fractions (10–40%) with grain sizes ranging from 150 to 400 μm, whereas pyroxene is present in smaller quantities (1–12%) with derived grain sizes ranging from 100 to 200 μm. Most of the hydrated phases such as kieserite, epsomite, ferrihydrite, schwertmannite, and nontronite are fine grained (~5–30 μm). One exception is jarosite, which has modeled grain sizes ranging from 200 to 300 μm. Other phases such as opaline silica have intermediate grain sizes around 140 μm. Note that the RMS errors reported here are the uncertainties from the NNLS model that is derived from the covariance matrix, and a detailed laboratory study is needed to understand the true scale of the errors although some laboratory work using binary mixture has provided encouraging initial results [Robertson *et al.*, 2016].

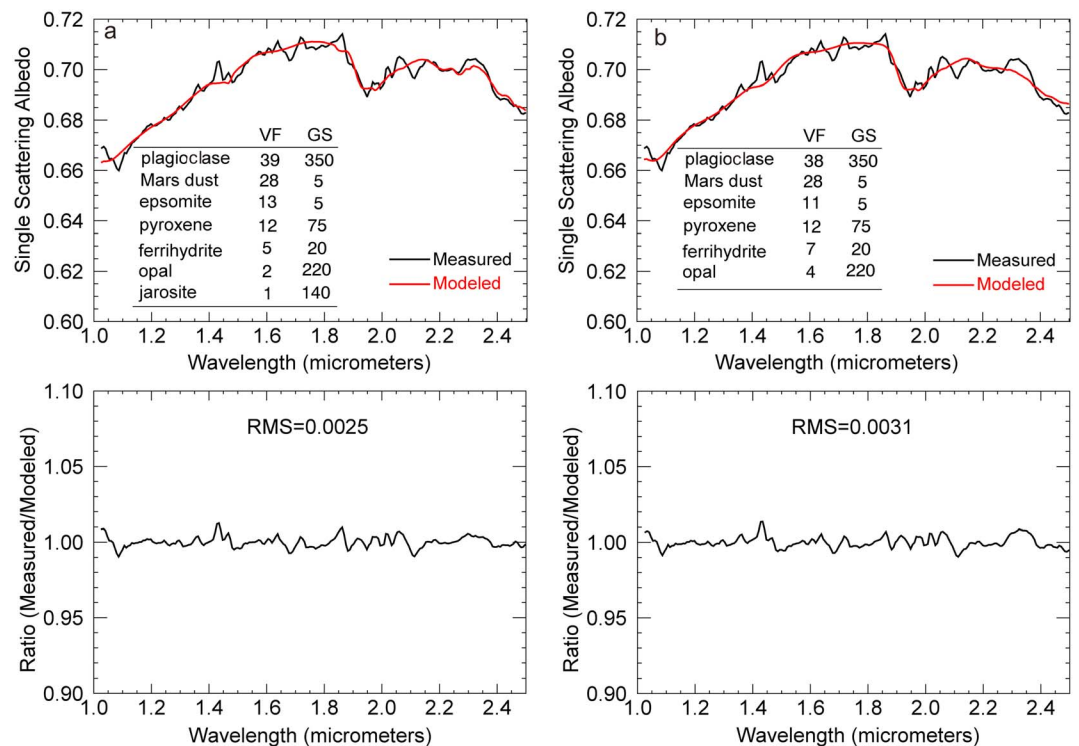


Figure 7. Mineral abundances and grain sizes for spot #1: Polyhydrated sulfates in the interbedded unit 1. (a) With jarosite included in the model. (b) With jarosite excluded in the model. RMS and derived abundances and grain sizes for the end-members are indicated. VF = volume fraction in percent, GS = grain size in micrometers.

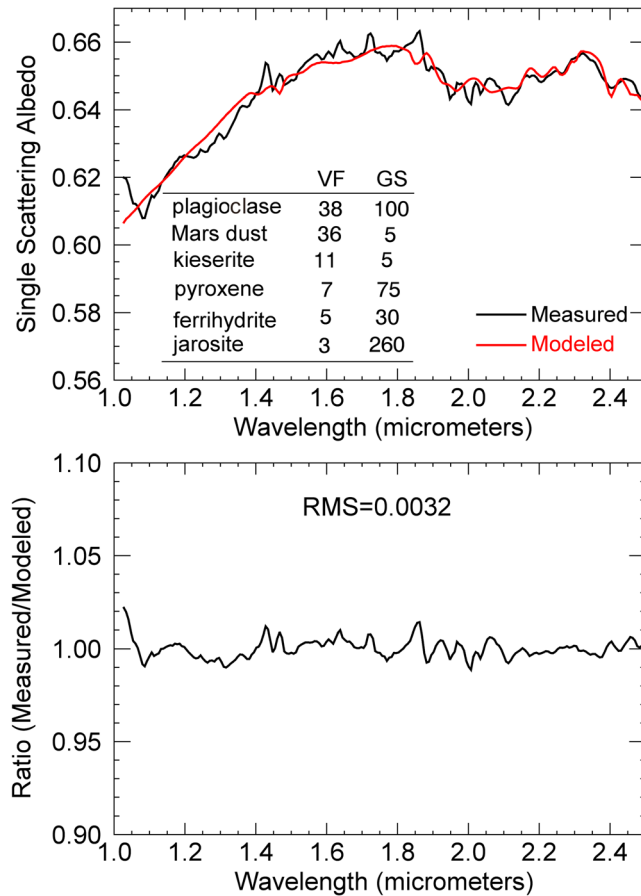


Figure 8. Mineral abundances and grain sizes for spot #2: Monohydrated sulfates in the interbedded unit 1.

sulfates with different cations and/or different hydration states preclude the identification of a specific phase. In this study we use epsomite as the proxy hydrous end-member to model the spectra with polyhydrated sulfate signatures. Note that in the most polyhydrated-sulfate-rich pixels, the spectra show multiple shallow absorption features around 2.2–2.3 μm, which may be due the presence of minor jarosite and/or opaline silica. Also, note that there is a spurious absorption feature around 2.103 μm in most of the retrieved CRISM spectra from FRT00013F5B, which is an artifact produced in the SSA retrieval with DISORT modeling. Example spectral unmixing results for areas with polyhydrated sulfates in the interbedded unit 1 are shown in Figure 7a, where an abundance of ~13% epsomite gives the best fit (RMS = 0.0025) to the measured spectrum. A small amount of jarosite and opaline silica (3% by volume) can reproduce the bands in 2.2–2.3 μm region; in contrast, if jarosite is removed from the spectral library, the modeled spectrum fails to reproduce the absorption features between 2.2 and 2.3 μm as well as the reflectance drop from 2.3 to 2.4 μm (Figure 7b), and the RMS increases by 20%. The spectral unmixing results also show that there is 5% ferrihydrite with a grain size of 20 μm. Note that although ferrihydrite is a nanomaterial and typically forms in nanophase, this material is hygroscopic, resulting in individual nanoparticles clumping together to form an effective single scatter. Therefore, we argue that it is reasonable to use bigger grain size such as 20 μm in our model. Ferrihydrite is present in most of the model results to reproduce the ferric band in 1.0–1.3 μm and to adjust the intensity of the 1.9 μm band [Poulet *et al.*, 2008]. In addition to the hydrous phases, the deposits also contain substantial igneous primary minerals, including 39% plagioclase and 12% pyroxene.

4.2.1.2. Monohydrated Sulfates in the Interbedded Unit 1

Monohydrated sulfates with only one H₂O per unit cell are characterized by absorption features at ~1.6 and 2.1 μm and by a narrow absorption feature at ~2.39 μm in addition to the reflectance drop between 2.3 and 2.4 μm. There are two monohydrated sulfate phases, kieserite (MgSO₄ · H₂O) and szomolnokite (FeSO₄ · H₂O),

In addition to modeling average unit spectra, we investigated the spatial distribution of mineral species by applying our spectral unmixing model to the entire image cubes and deriving mineral abundance maps. The abundance maps of hydrous phases including hydrated sulfates, jarosite, and Fe-smectites were generated and compared to the CRISM parameter index maps. We were also able to evaluate the correlation between the model abundances and the index maps. Using the derived mineral abundances, we aim to better understand the formation mechanisms of hydrated mineral assemblages in the study area.

4.2.1. Spectral Unmixing Results for Individual Spectra

4.2.1.1. Polyhydrated Sulfates in the Interbedded Unit 1

The interbedded hydrated sulfate unit, as outlined by the white box in Figures 4a and 4b, contains alternating layers of polyhydrated and monohydrated sulfates (Figure 4c). Polyhydrated sulfates with multiple H₂O molecules per unit cell are identified by absorption features at ~1.4 and 1.9 μm as well as a reflectance drop at ~2.4 μm. The spectral similarities between polyhydrated

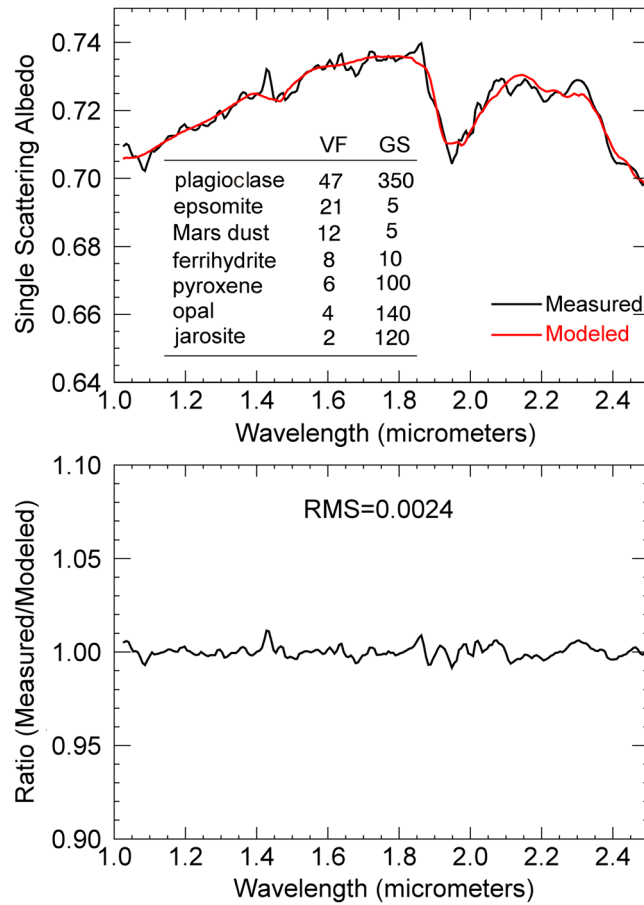


Figure 9. Mineral abundances and grain sizes for spot #3: Polyhydrated sulfates outside the interbedded unit 1.

from the interbedded unit 1, the polyhydrated sulfates exposed in this unit have a much deeper absorption band around 1.9 μm, which implies a relatively higher volume fraction in abundance. Another difference is that although the spectra from both units have multiple shallow bands in the 2.2–2.3 μm wavelength region, the spectra from this unit have a relatively deeper absorption band around 2.2 μm. This indicates that there might be more opaline silica in this spot than the spot in the interbedded unit 1. Example unmixing results are shown in Figure 9, and our modeling results are consistent with visual inspection of the band depths. The epsomite in this unit is modeled with 21% abundance, with ~4% opaline silica and 8% ferrihydrate. Primary igneous minerals include plagioclase with an abundance of 47% and pyroxene with an abundance of 6%.

4.2.1.4. Monohydrated Sulfates Outside the Interbedded Unit 1

The monohydrated sulfates outside the interbedded unit 1 are exposed on a bench unit and on the top of the areally extensive polyhydrated sulfate units (Figure 4b). Similar to the polyhydrated sulfates discussed in section 4.2.1.3, monohydrated sulfates in the bench unit have a deeper water band around 2.1 μm than that in the interbedded unit 1. The unmixing results indicate that there is ~14% kieserite in this unit (Figure 10a). A small amount of jarosite (4%) is required to account for the shallow absorption bands around 2.265 μm, and our modeling results show that removing jarosite from the spectral library results in substantially larger RMS error (increasing from 0.0028 to 0.0046) and a visually poorer fit (Figure 10b). Other phases in this spot include 41% plagioclase and 5% pyroxene.

4.2.1.5. Jarosite-Bearing Unit 1

Jarosite is exposed in the capping units to the north of the interbedded unit 1 (Figure 4b) and was identified by the absorption features at ~1.48, 1.85, and 2.265 μm. As the 2.265 μm band is the most important diagnostic feature for jarosite, its band depth is directly correlated to the derived abundance of jarosite. Thus, properly modeling the shape and band depth around 2.265 μm is required to more accurately estimate

that can be distinguished from each other based on the variations of absorption features around 2.1 μm. For example, kieserite spectra have a doublet at 2.06 and 2.13 μm, whereas szomolnokite spectra show a singlet at 2.09 μm. Inspection of the monohydrated sulfate spectra in the study area shows that they are more consistent with kieserite. Thus, we use kieserite as the primary hydrous end-member to model the spectra with monohydrated sulfate signatures in this study. Example unmixing results for areas with monohydrated sulfates in the interbedded unit 1 are shown in Figure 8. The CRISM spectrum over this unit has a lower signal-to-noise ratio, which has resulted in a larger RMS (0.0032) in the modeling. The modeling results indicate that an 11% volume fraction of kieserite gives the best fit. Ferrihydrate has a similar abundance (5%) as spot #1, as does jarosite (3%). The primary minerals also have large volume fractions with 38% plagioclase and 7% pyroxene present.

4.2.1.3. Polyhydrated Sulfates Outside the Interbedded Unit 1

Outside the interbedded unit 1 is an areally extensive polyhydrated sulfate-bearing unit shown as red in Figure 4b. Compared to the polyhydrated sulfate

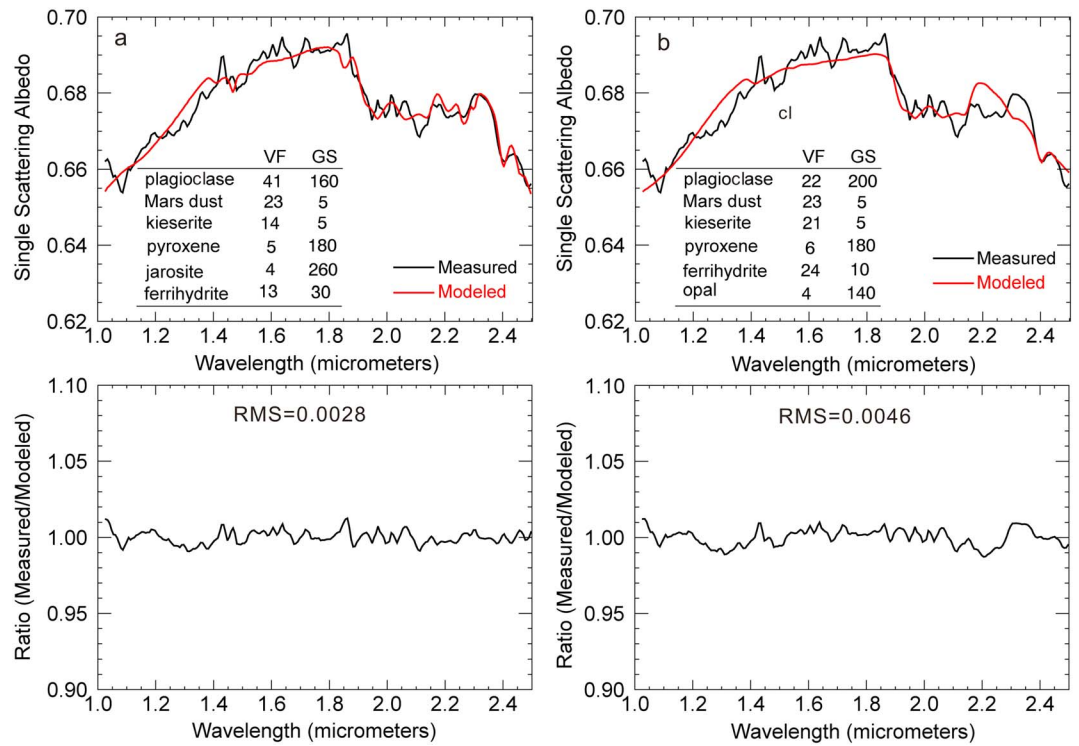


Figure 10. Mineral abundances and grain sizes for spot #4: Monohydrated sulfates outside the interbedded unit 1. (a) With jarosite included in the model. (b) With jarosite excluded in the model.

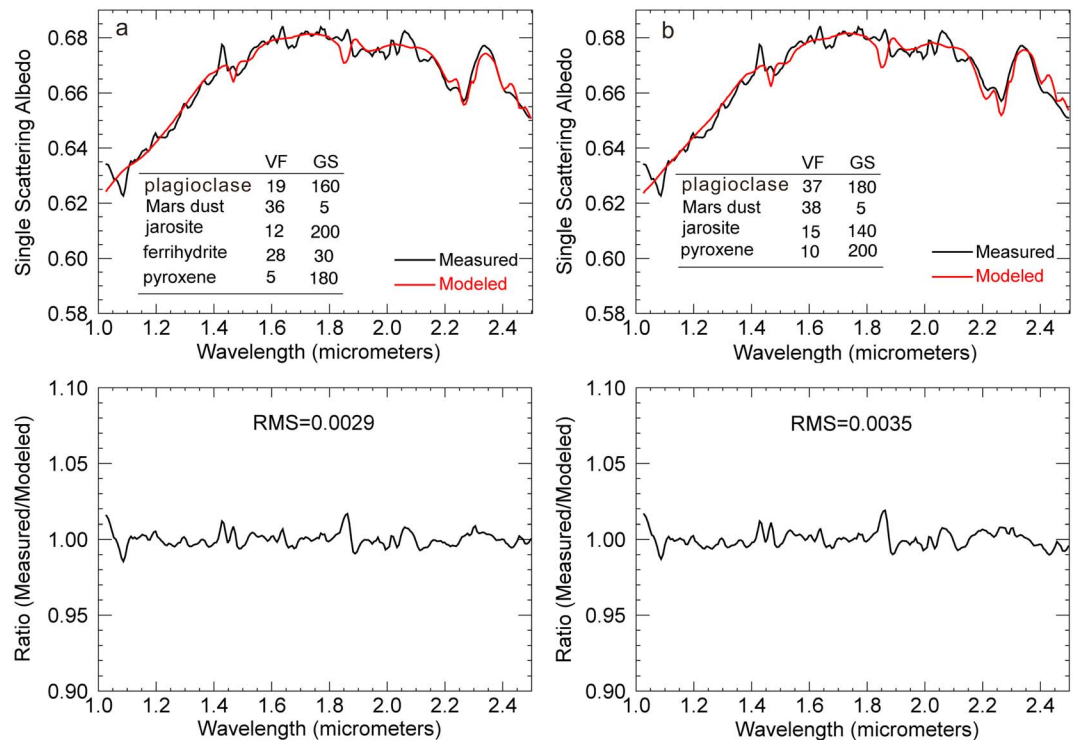


Figure 11. Mineral abundances and grain sizes for spot #5: Jarosite in the jarosite-bearing unit 1. (a) With ferrihydrate included in the model. (b) With ferrihydrate excluded in the model.

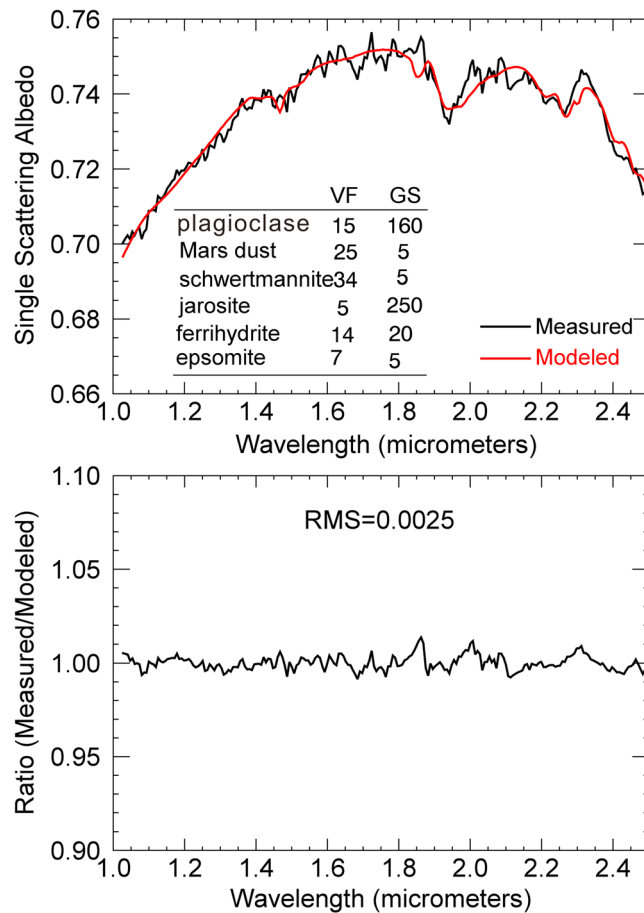


Figure 12. Mineral abundances and grain sizes for spot #6. The representative spectrum has both 1.93 and 2.265 μm bands and was taken from the jarosite-bearing unit 2.

phase is present in addition to jarosite. In our spectral unmixing modeling, several end-members were considered that can produce the 1.9 μm feature and are generally featureless in other spectral regions. These end-members include epsomite, ferrihydrate, goethite, and schwertmannite. The spectral unmixing results from this unit (Figure 12) reveal a complex hydrous assemblage. Hydrated phases including schwertmannite, ferrihydrate, jarosite, and epsomite are all present, of which schwertmannite has largest volume fraction of 34% with very fine (5 μm) grains. Other phases include 14% ferrihydrate and 7% epsomite in this unit. Modeling results show jarosite only has a volume fraction of 5%, which indicates that a small amount of jarosite can produce the strong and diagnostic absorption features around 2.265 μm . Similar to jarosite-bearing unit 1, jarosite-bearing unit 2 contains relatively minor amounts of primary igneous minerals, with only 15% plagioclase present.

4.2.1.7. Phyllosilicates in the Interbedded Unit 2

Phyllosilicates have diagnostic absorption features from 2.1 to 2.5 μm due to metal-OH combination stretching and bending vibrations associated with different types of cations in the octahedral site [Clark *et al.*, 1990]. CRISM spectra over the phyllosilicate-rich area in the interbedded unit 2 (Figure 4e) show an absorption band around 2.29 μm in addition to a 1.9 μm water band, which is mostly consistent with Fe-smectites (i.e., nontronite). Example unmixing results are shown in Figure 13, and the best fit model spectrum requires at least 39% nontronite in the system. Note that our best fit was not able to perfectly produce the depth and the wings of the 2.29 μm feature but still provides RMS value that is less than 0.003. Also, the CRISM spectra from this unit include a shallow absorption feature around 2.1 μm , and our modeling results indicate that the presence of 6% kieserite can account for this band. This is because the 10 \times 10 pixel size may have included a portion of the sulfate-bearing layer. The primary minerals have less than 50% abundance with 25% plagioclase and 11% pyroxene.

the concentration of jarosite in this area. We start by modeling the average spectrum over the jarosite deposits with only anhydrous primary phases (plagioclase, pyroxene, and Mars dust) as well as the jarosite end-member, and the modeling results show that even the best fit can give RMS values as large as 0.0035 (Figure 11b). Also, the model spectrum has a deeper absorption feature at 2.265 μm than the measured spectrum. However, when ferrihydrate is added to the end-member library, the RMS value is reduced to 0.0029 and the model spectrum can reproduce the 2.265 μm band in both the shape and the depth (Figure 11a). The unmixing results indicate that there is ~12% jarosite and a substantial amount of ferrihydrate with a modeled abundance of 28% in this unit. Also, the modeled abundances of primary minerals are substantially reduced compared to the polyhydrated and monohydrated sulfate units, with only 19% plagioclase and 5% pyroxene.

4.2.1.6. Jarosite-Bearing Unit 2

Close to the jarosite-bearing unit 1, there is a unit showing spectra with both a deep 1.93 μm water band and a 2.265 μm band. This unit is displayed in purple in the composite CRISM parameter map (Figure 4b). The deep 1.9 μm band indicates that a hydrous

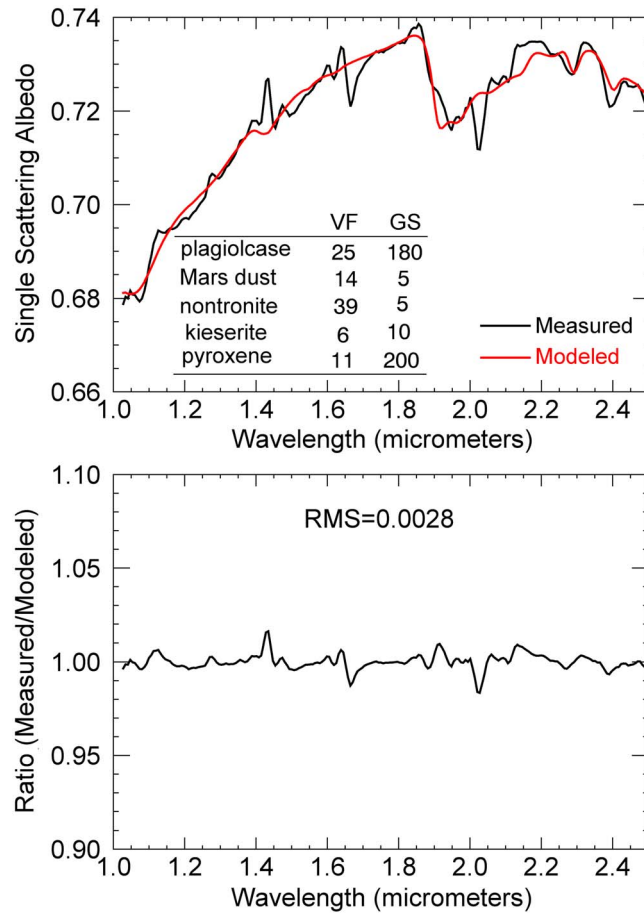


Figure 13. Mineral abundances and grain sizes for spot #7: Phyllosilicates in the interbedded unit 2.

4.2.1.8. Polyhydrated Sulfates in the Interbedded Unit 2

Hydrated sulfates within the interbedded unit 2 have both polyhydrated and monohydrated sulfate phases. The spectra from the polyhydrated-sulfate-rich spot have a deep absorption feature around 1.9 μm and a shallow absorption band around 2.1 μm. Our spectral unmixing results for this spot are shown in Figure 14, which indicates that there is ~19% epsomite and ~10% kieserite present. In addition, there is a significant amount of ferrihydrite with a volume fraction of 25%. Primary minerals have a total abundance of 37%.

4.2.1.9. Monohydrated Sulfates in the Interbedded Unit 2

Example unmixing results for the monohydrated sulfate-rich spot in the interbedded unit 2 are shown in Figure 15, where the best fit effectively reproduces the spectral shape and absorption features around 2.1 and 2.4 μm of the CRISM spectrum and has a RMS value as low as 0.0024. The monohydrated sulfates (i.e., kieserite) have an abundance of 25% in this unit. Similar to the polyhydrated-sulfate-rich unit in the interbedded unit 2, this unit contains a substantial amount (21%) of

ferrihydrite. In contrast, there is higher modeled abundance of primary minerals, with 42% plagioclase and 12% pyroxene.

4.2.2. Quantitative CRISM Mineral Abundance Maps

To investigate spatial distribution of the hydrated mineral abundances in southwest Melas Chasma, we applied our spectral unmixing model to CRISM images FRT00013F5B and HRL0001900F, generating a series of mineral abundance maps. Pixel by pixel scatterplots of CRISM index value [Viviano-Beck et al., 2014] versus derived mineral abundance were also produced to evaluate the correlation between them. The derived mineral abundance maps of jarosite, hydrated sulfates (both polyhydrated and monohydrated sulfates included), and monohydrated sulfate for FRT00013F5B together with their index maps are shown in Figures 16–18, respectively. To some extent, the mineral abundance maps generated from the model agree well spatially with CRISM-derived parameter maps [Viviano-Beck et al., 2014]. Particularly, for the jarosite end-member, the derived jarosite map nicely matches the index map of BD2265 for the entire scene, and the scattering plot also shows great correlation (Figure 16). However, a discrepancy exists between the two sets of maps particularly for hydrated sulfates. For example, for the hydrated sulfate maps (both polyhydrated and monohydrated sulfate included) as shown in Figure 17, the model abundance map fails to reproduce the enhanced brightness in the lower right part of the SINDEX2 index map. Examination of the spectra from these regions shows polyhydrated sulfate signatures, which indicates that our model might underestimate the abundance of polyhydrated sulfates, indicating potential limits in our ability to adequately model this phase. A possible explanation is that our spectral library used for the unmixing model may lack some polyhydrated sulfate phases that are present in these regions and can be mapped by CRISM SINDEX2 index. For the monohydrated sulfate maps, the derived model abundance agrees well with the index map only around the bench unit as labeled in Figure 4b, and the scatterplot shows a fairly poor correlation

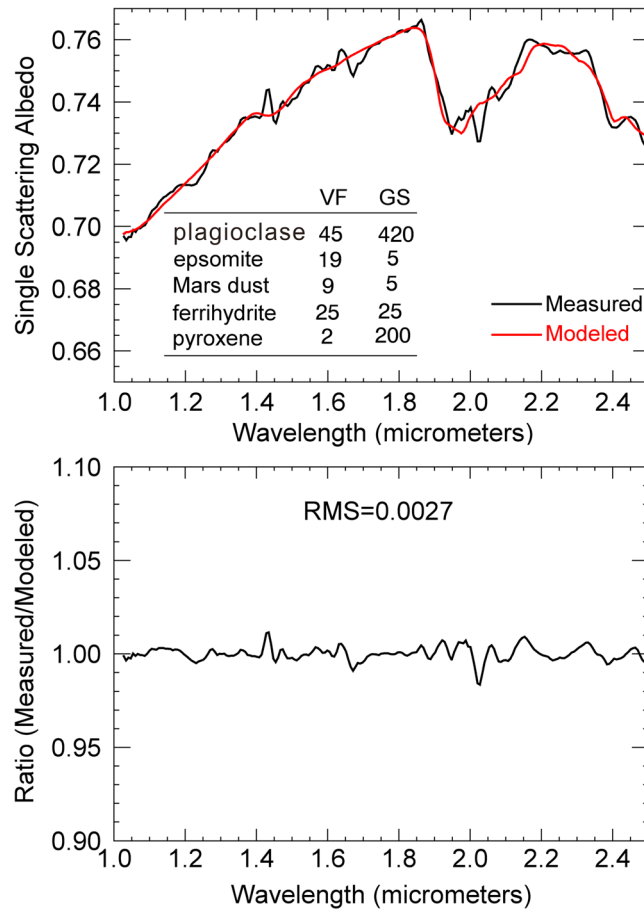


Figure 14. Mineral abundances and grain sizes for spot #8: Polyhydrated sulfates in the interbedded unit 2.

index maps are shown in Figures 20 and 21. Again, the derived model abundance agrees well with the index map to some extent. For example, enhanced brightness is observed in the interbedded unit for both hydrated sulfate and phyllosilicate maps. Similar to FRT00013F5B, discrepancies exist between the index and model abundance maps. This is either because the model fails to accurately recognize minerals below a detection limit or because the CRISM data are too noisy, as these two images were taken by an aged CRISM instrument with limited data quality. Future work is needed to improve the model results by updating the spectral library end-members, improving the accuracy of the single-scattering albedos, and smoothing CRISM images before unmixing.

5. Error Analysis and Sensitivity Tests

In this section, we discuss possible error sources and describe sensitivity analyses on these sources. In addition, we estimate the statistical error on the model abundances.

5.1. Errors From the Modeling Approach

One source of the error comes from the unmixing modeling technique performed in this study. The root-mean-square (RMS) is used to evaluate the difference between values predicted by a model and the values actually observed. In addition to low RMS values, assessment of the quality of a model fit of a spectrum by visual inspection is also needed [Poulet et al., 2014]. Determining the accuracy of the unmixing model is important and requires laboratory testing of the mixtures. The preliminary testing of the modeling approach used in this study has been performed on a variety of single, two, and three-mineral mixtures of pyroxene, plagioclase, and olivine [Scudder et al., 2015]. Although relatively large variation has been obtained for the

(Figure 18). For example, the BD2100 index map (Figure 18a) shows substantial amount of monohydrated sulfates in the low middle part of the scene (i.e., the plateau), whereas the model abundance map (Figure 18b) clearly shows that there are no monohydrated sulfates present in the same area. One possible reason is that the presence of high-calcium pyroxene (HCP) which has a broad absorption feature around 2.1 μm may have contributed to the BD2100 index. To test this hypothesis, we also modeled HCP abundances. The model abundance and HCPINDEX2 index maps show great consistency (Figure 19). Comparison between Figures 18 and 19 indicates that the additional enhancement in BD2100 index map as compared to the model monohydrated sulfate abundance map is probably due to the contributions of HCP to the BD2100 index map. The BD2100 index map clearly overestimates the distribution and the abundance of the monohydrated sulfate when HCP is present as a major phase. Thus, caution should be used when mapping monohydrate sulfates using CRISM BD2100 index.

The derived mineral abundance maps of hydrated sulfates and phyllosilicates for HRL0001900F together with their

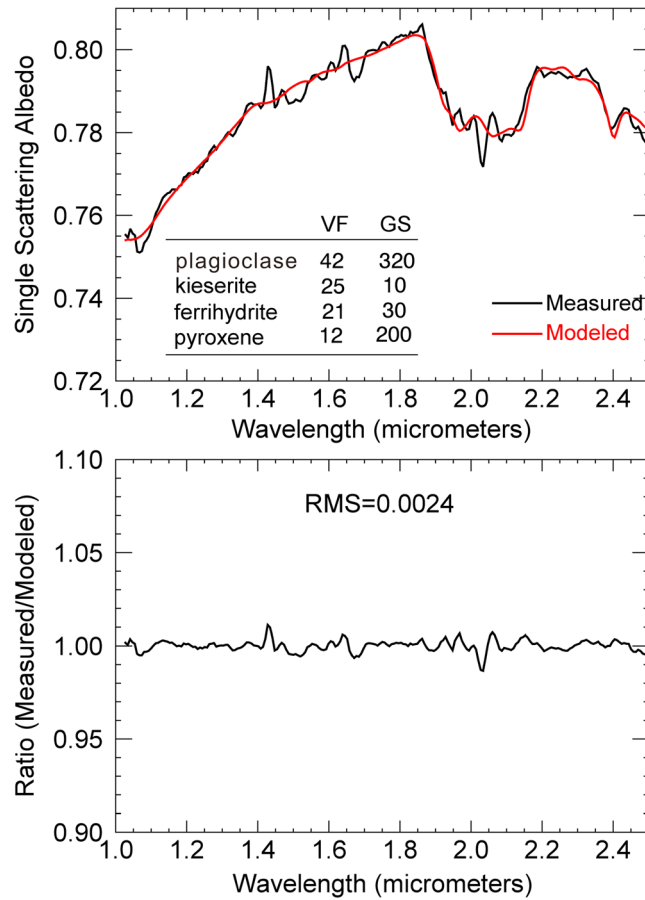


Figure 15. Mineral abundances and grain sizes for spot #9: Monohydrated sulfates in the interbedded unit 2.

different regions [Poulet *et al.*, 2014]. We selected two spectra from two clean regions in FRT00013F5B containing extensive polyhydrated sulfate signatures to perform spectral unmixing analysis. The model results indicate that the model abundances for the two regions have variations of 2% for epsomite, 5% for ferrihydrite, 11% for plagioclase, 3% for pyroxene, and 5% for Mars dust (Figure 22). The variations in grain size are mostly related to the primary minerals, i.e., a 60 μm difference for plagioclase and a 50 μm difference for pyroxene. Other phases have similar grain sizes. Overall, these variations are small and within the expected discrepancies.

5.2. Errors From Grain Size Selections

Another source of the error comes from the uncertainties of the selection of the grain size in the unmixing model. Grain size is an important parameter that controls the amount of light scattered and absorbed by a grain and can affect both the shape and the depth of the absorption features [e.g., Hapke, 1993]. Constraints must be given to the grain sizes so that more control over the process of minimization is exerted by avoiding unrealistic grain sizes to obtain more reliable results. Grain sizes of the materials on the Martian surface can be estimated from the thermal inertia [e.g., Edgett and Christensen, 1991]. The thermal inertia data from Putzig and Mellon [2007] show that the study area has relatively large thermal inertia values ranging from 200 to 400 $\text{Jm}^{-2}\text{K}^{-1}\text{s}^{-1/2}$, corresponding to coarse-grained materials.

To test the sensitivity of our spectral unmixing model to the grain size of the library end-members, we modeled the spectrum from the polyhydrated sulfate unit outside the interbedded unit 1 (spot #3) as an example to demonstrate how grain size selection affects the model results and how to use thermal inertia data to guide grain size selection in order to reduce the error. First, we ran model with the grain size as a free parameter with a wide range from fine (<30 μm) to coarse (>300 μm) grains. The model results show

primary minerals especially for the spectrally featureless plagioclase, the model variation can become small for the altered minerals with more diagnostic absorption features. For example, a recent laboratory study by Robertson *et al.* [2016] shows that the model error was within 5%, in which they estimated model abundances of clay-gypsum mixtures using a revised Hapke VIS-NIR and Shkuratov radiative transfer model. Also, these laboratory studies indicate that our derived mineral abundances for end-members with low spectral contrast such as plagioclase, pyroxene, and ferrihydrite may have lower accuracy than that of hydrated mineral phases, and additional laboratory studies on modeling more complicated systems including end-members with both high and low spectral contrasts are needed to understand their model accuracies.

A full laboratory study on the testing of spectral unmixing of the mixture with multiple components is beyond the scope of this work. Alternately, we evaluate the uncertainties on the mineral abundances and grain sizes by comparing the derived values for the two spectra with similar spectral shape and absorption features extracted from two

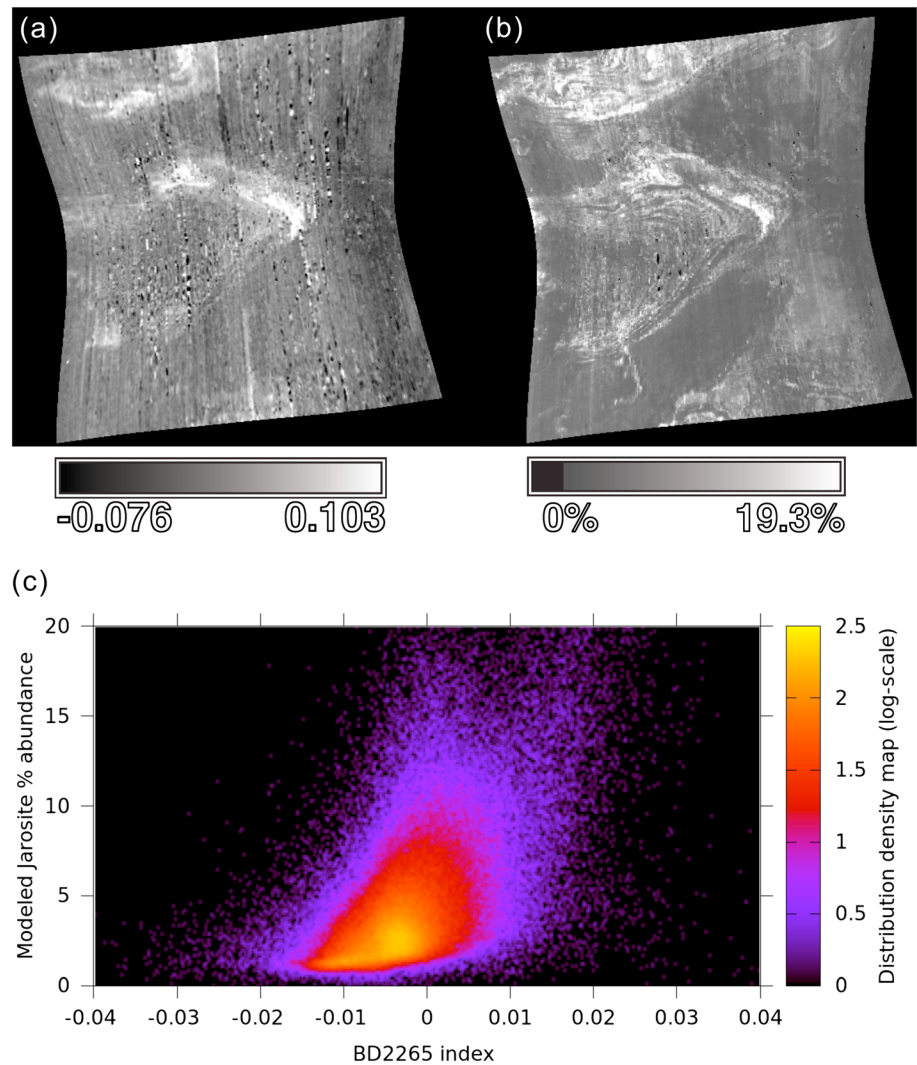


Figure 16. Comparison between CRISM parameter index map and derived abundance map for jarosite in FRT00013F5B. (a) BD22265. (b) Model jarosite abundance. (c) Correlation between the model abundances and the index maps.

that the best fit has fine grain sizes ($<30\ \mu\text{m}$) both for altered minerals (i.e., epsomite) and primary minerals (i.e., plagioclase and pyroxene) with a RMS of 0.0021 (Figure 23a). In this case, the model gives better fit (i.e., lower RMS) than that shown in Figure 9. However, thermal inertia data show that the grain size in this area should be coarser than $200\ \mu\text{m}$, which contradicts with model results. Thus, the best spectral fit with lowest RMS does not necessarily imply the best assessment of model abundance or grain sizes (if, in fact, the thermal inertia in this region is directly correlated with grain size). We then reran model with three combinations of grain size selections: (1) coarse-grained ($>200\ \mu\text{m}$) altered minerals and fine-grained ($<30\ \mu\text{m}$) primary minerals, (2) coarse-grained altered minerals and coarse-grained primary minerals, and (3) fine-grained altered minerals and coarse-grained primary minerals. The coarse-grained end-members are included in all of the three cases to make the grain size to be consistent with the thermal inertia data. The model results show that both case (1) and case (2) give large RMS errors (0.0041 and 0.0047, respectively), whereas case (3) gives a satisfactory RMS error (0.0024) (Figures 23b–23d). Thus, grain size selection can largely affect model results, and constraining grain size based on other factors such as the thermal inertia data is important to produce more reliable results. One should also note that limitations exist on constraining the grain size due to much coarser resolution of thermal inertia data as compared to the CRISM data. Further constraints on the grain size are needed when higher-resolution thermal inertia data are available.

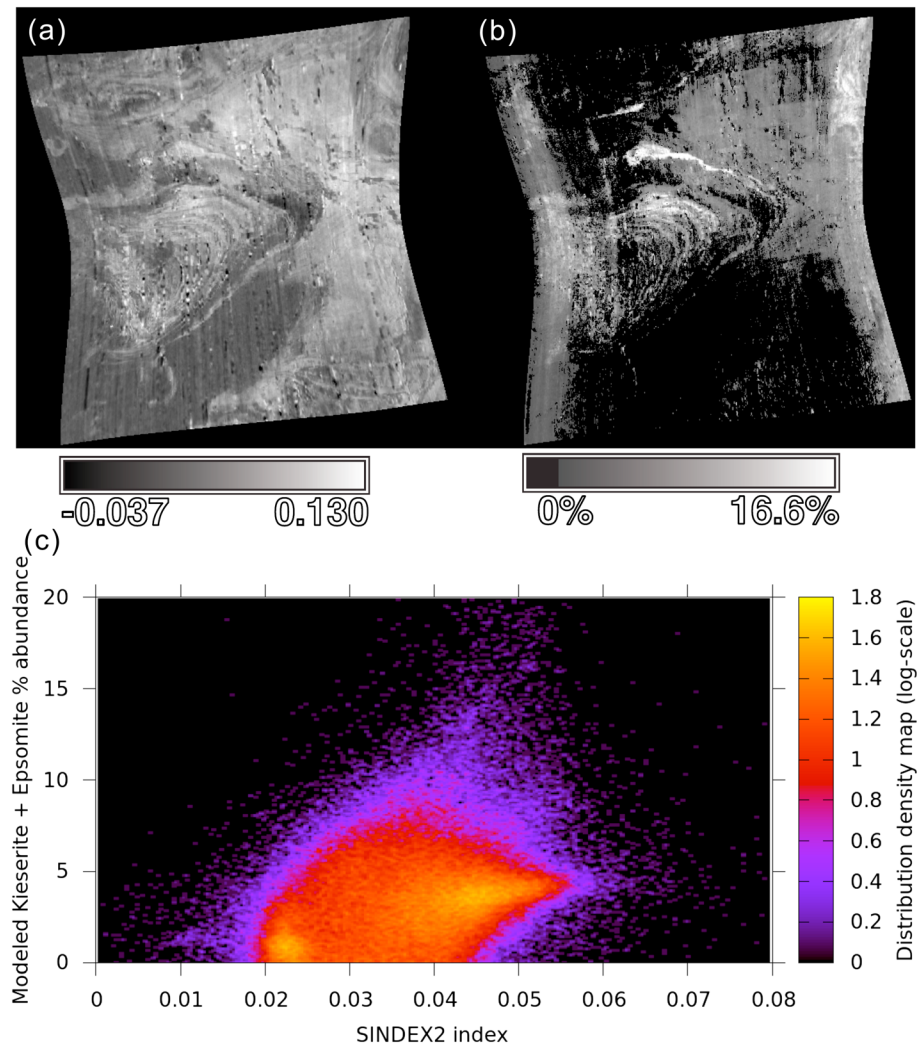


Figure 17. Comparison between CRISM index map and derived abundance map for hydrate sulfates in FRT00013F5B. (a) SINDEX2. (b) Model sulfate abundance. (c) Correlation between the model abundances and the index maps.

5.3. Errors From End-Members Selections

We do not have a priori knowledge of the exact constituents of a mixed spectrum; thus the end-members selected to perform unmixing can cause errors in the derived abundances. In this study, we use the FATT technique, visual inspection, and previous knowledge of Martian geologic processes and evolution to make our decisions on the major components used in our unmixing models. Some sensitivity tests were performed, and the results have been discussed in section 4.2.1. In this section we add two additional sets of sensitivity tests on the slope end-members and plagioclase end-member used in the unmixing model, respectively.

Slope end-members have been used in our model as well as other researcher's work [e.g., Adams *et al.*, 1986; Combe *et al.*, 2008; Poulet *et al.*, 2009] to improve the fitting. We performed sensitivity testing on the model results by excluding slope end-members using the spectra with polyhydrated sulfate, monohydrated sulfate, and jarosite signatures, and the results are displayed in Figure 24. Compared to the initial model results that included slope end-members shown in Figures 7, 10, and 11, the RMS values have increased and the abundances have changed a bit (within 5%) but not dramatically. That being said, slope end-members help improve the fit but have no large effects on our model abundances on the end-members derived in this study. However, these tests are not exhaustive, and future implementation of mixing models using these convenience end-members warrants further study to determine the conditions where the effects are large (i.e., when modeling end-members with low spectral contrast).

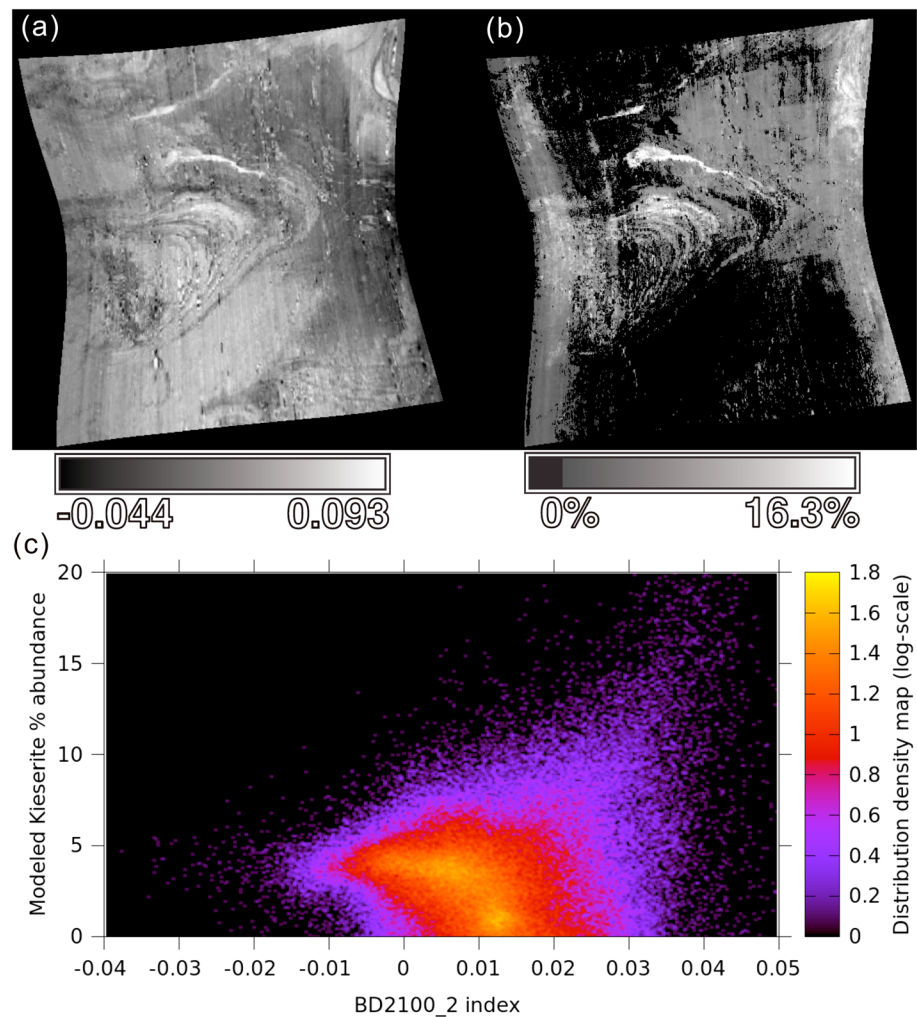


Figure 18. Comparison between CRISM index map and derived abundance map for monohydrate sulfates in FRT00013F5B. (a) BD2100_2. (b) Model kieserite abundance. (c) Correlation between the model abundances and the index maps.

The plagioclase end-member used in this study has minor contamination possibly from muscovite and shows some absorption features due to the water in the crystal structure of muscovite. In our sensitivity tests, plagioclase was not excluded as this phase is a common material in basalt and should be included in the modeling. Instead, we manually modified the optical constants of plagioclase in our spectral library to remove these absorption features due to hydrated phases and then reran the spectral unmixing model to see how the model abundances change. We performed sensitivity test on the model results using the spectra with monohydrated sulfate, jarosite, and smectite signatures, and the results are shown in Figure 25. Compared to the model results using the contaminated plagioclase spectrum as shown in Figures 10, 11, and 13, there are some changes to the derived mineral abundances but again, they are not significant.

5.4. Errors From Albedo Inversion Model

The uncertainties in the retrieval of the single-scattering albedos using DISORT can also cause bias in model results. To correctly derive the mineral abundances and grain sizes using the retrieved single-scattering albedos, the DISORT model used to derive the single-scattering albedos must be validated. Fortunately, the approach has been validated by retrieving similar albedos over the same areas using different observations [Liu *et al.*, 2012b]. For example, we used OMEGA observations ORB0401_3 and ORB1326_1 to evaluate the modeling approach through comparing the retrieved Lambert albedo over the same area. The two scenes were acquired at different times, atmospheric conditions, lighting and viewing geometries but have overlapped coverage. The results show that the retrieved Lambert albedos are similar both in spectral shape and

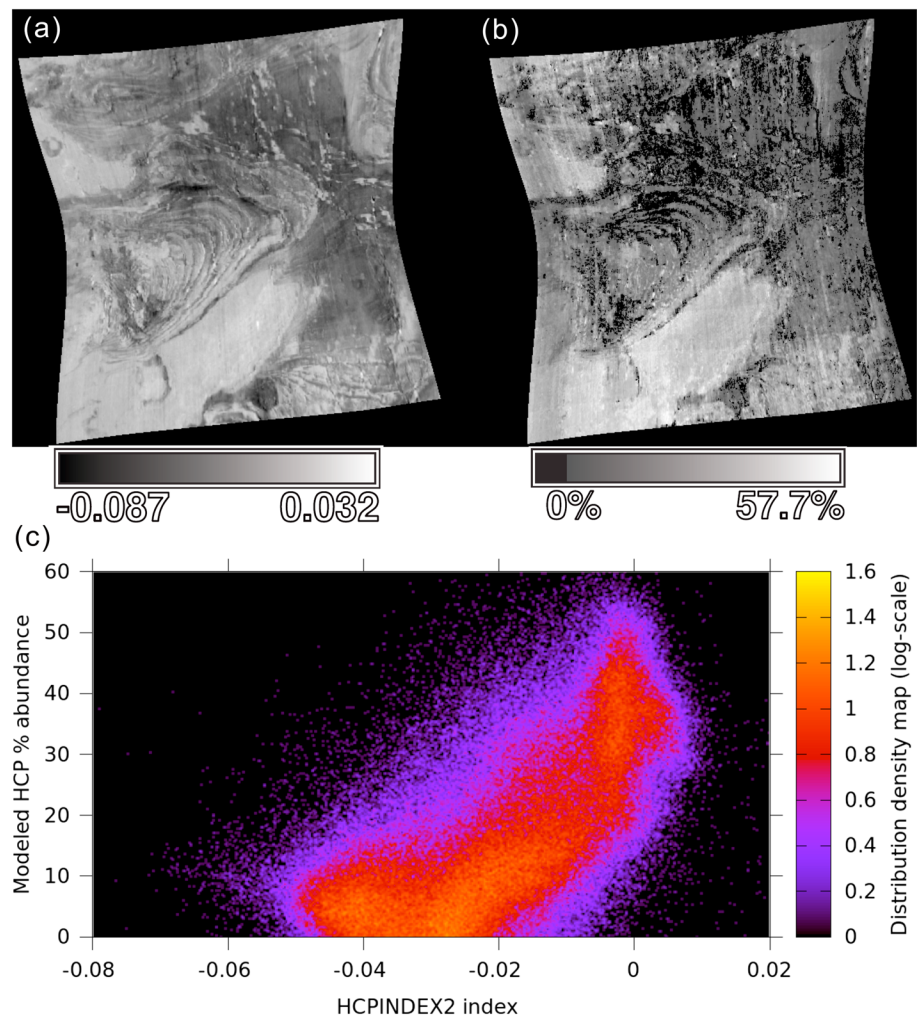


Figure 19. Comparison between CRISM index map and derived abundance map for high-calcium pyroxene (HCP) in FRT00013F5B. (a) HCPINDEX2. (b) Model HCP abundance. (c) Correlation between the model abundances and the index maps.

absolute values with a variation less than 0.5%. Similarly, using CRISM observations FRT00013F5B and FRT00023420 that cover the same area, we retrieved the single-scattering albedos and found the variations are also very small, and results will be reported in another paper. Thus, the uncertainties in the retrieved albedos using the DISORT modeling have only a minor contribution to the variation of the spectral unmixing results.

5.5. Statistical Error Estimate

Finally, we estimated statistical error in model end-member abundances following the approach described by *Rogers and Aharonson* [2008]. Statistical error is given by standard deviation that is equal to the square root of the diagonal of the model parameter coefficient covariance matrix. The covariance matrix is weighed by the model calculated parameter misfit and calculated by equation (1) in *Rogers and Aharonson* [2008]. The statistical error of the model abundances for the end-members analyzed in section 4.2.1 (i.e., spots #1–9) is listed in Table 3. The uncertainties are within 3% for all the end-member listed. As suggested by *Rogers and Aharonson* [2008], statistical errors are not direct indicators of the quality of the spectral fit and should be used together with the RMS error and visual inspection to evaluate the quality of the model fit.

6. Discussion

The mineral abundances derived from our spectral unmixing model provide valuable information that helps constrain the formation mechanisms of hydrated minerals and local aqueous environment at our study area.

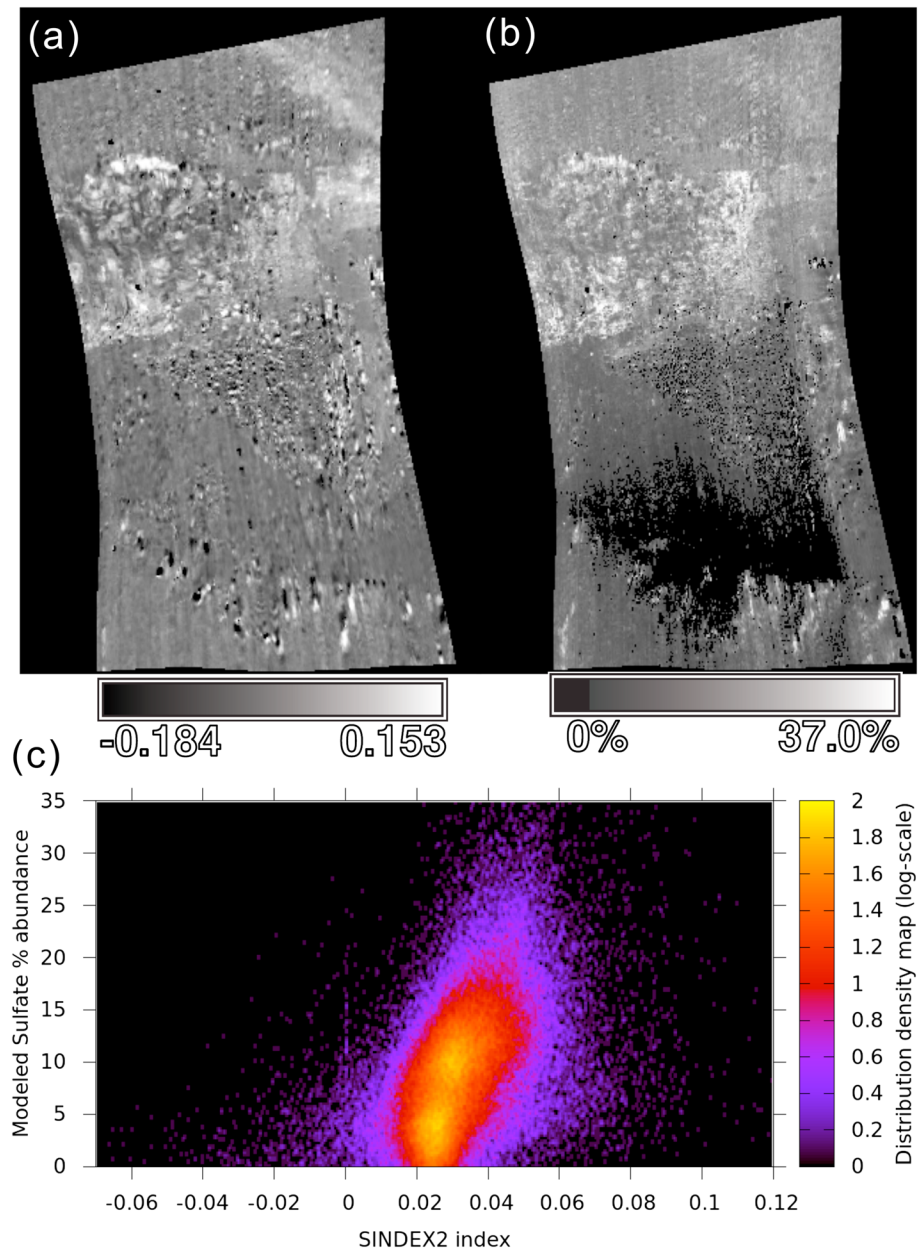


Figure 20. Comparison between CRISM index map and derived abundance map for hydrate sulfates in FRT0001900F. (a) SINDEXT2. (b) Model hydrated sulfate abundance. (c) Correlation between the model abundances and the index maps.

In southwest Melas Chasma, several mineralogically distinct units have been identified. Within the ILDs close to southern wall and nearby floor, a sequence of interbedded polyhydrated and monohydrated sulfates were found. Two hypotheses have been proposed to explain the interbedded sulfate layers, which were based on two different pathways for the formation of monohydrated sulfates (i.e., kieserite) at relatively low temperatures on Mars. One hypothesis is that they have formed by cyclic evaporation and precipitation of the two hydrated sulfate phases from two episodic brines with different water chemistry. Thermodynamic modeling performed by *Catalano et al.* [2012] indicates that although evaporation of fluids resulting from basalt weathering by a $\text{SO}_4\text{-Cl}$ solution does not form kieserite, a Cl-rich $\text{Mg-SO}_4\text{-Cl-H}_2\text{O}$ brine can facilitate the drop of the water activity and thus the precipitation of kieserite. Thus, a cyclic evaporation and precipitation sequence of polyhydrated sulfates forming at a high water-to-rock ratio and deposition of kieserite at a low water-to-rock ratio condition may have occurred. Another hypothesis is that the interbedded sulfates formed through

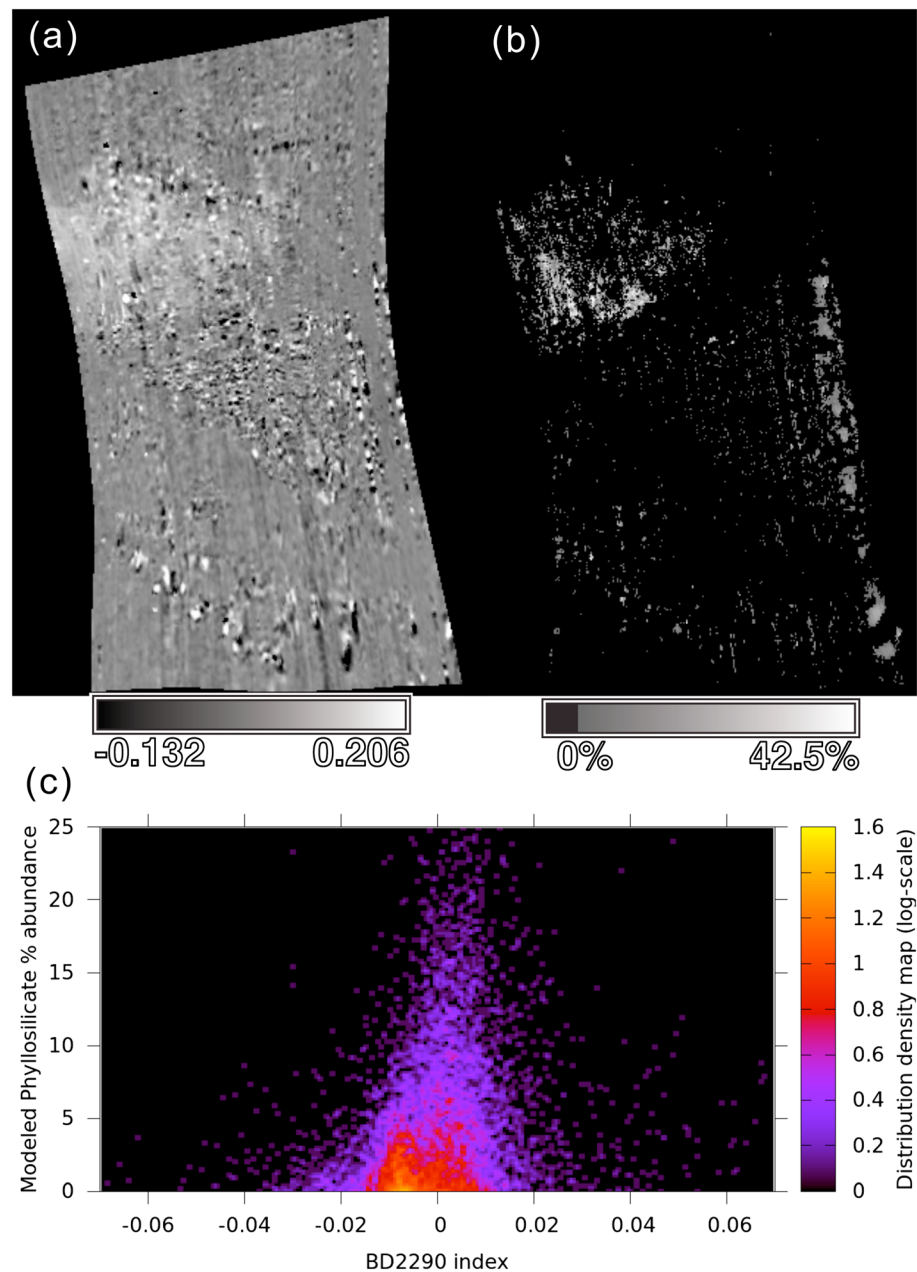


Figure 21. Comparison between CRISM index map and derived abundance map for phyllosilicates in FRT0001900F. (a) BD2290. (b) Model nontronite abundance. (c) Correlation between the model abundances and the index maps.

cyclic precipitation of polyhydrated sulfates and postdepositional dehydration into kieserite. Laboratory experiments conducted by *Wang et al.* [2016] show that a process containing two precipitation-dehydration stages can occur from a single complex Mg-Ca-Fe-SO₄-Cl brine, in which the early stage Mg sulfates dehydrated into kieserite whereas the later precipitated Mg sulfates did not fully dehydrate, resulting in the formation of starkeyite (MgSO₄·4H₂O). Thus, multiple inputs of chemically complex brines are capable of forming the interbedded polyhydrated and monohydrated sulfates observed in Melas Chasma.

Our spectral unmixing results indicate that the kieserite within the interbedded strata and outside the strata have similar abundances (11% and 14%, respectively), whereas polyhydrated sulfates within the interbedded strata are present at lower abundances (13%) than the surrounding areal polyhydrated sulfates (21%). As discussed in *Liu et al.* [2012a] and *Liu and Glotch* [2014], it is unclear whether the kieserite in the bench unit

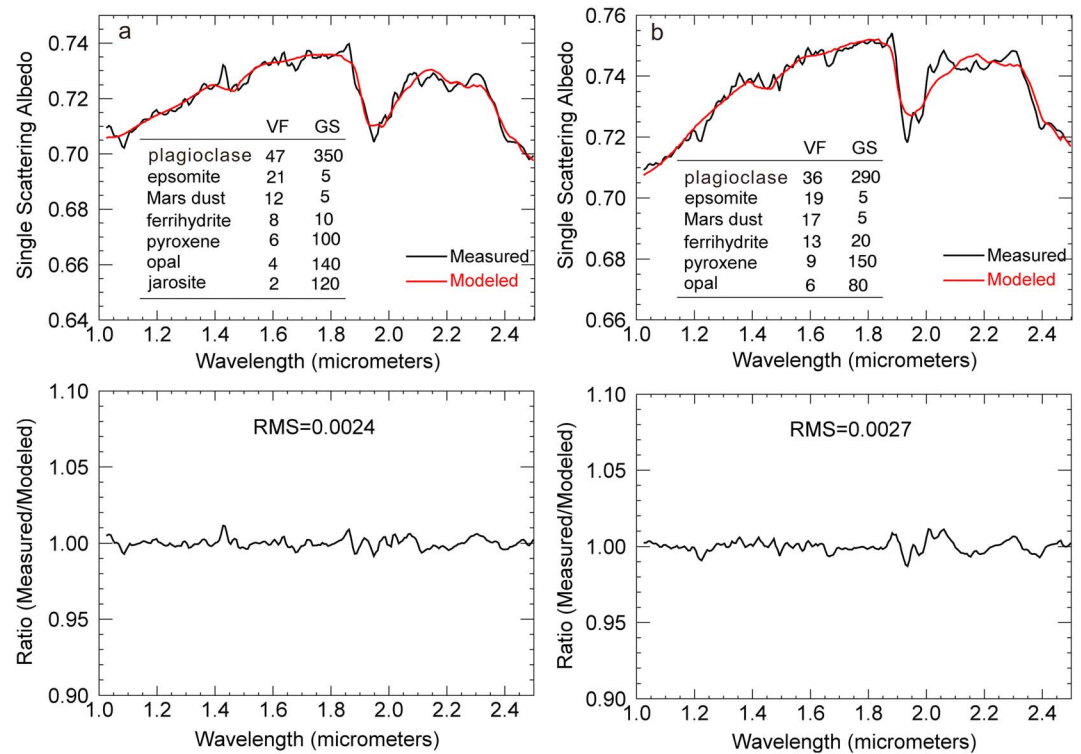


Figure 22. Comparison between the derived mineral abundances and grain sizes in two regions with extensive polyhydrated sulfates signatures. (a) The spectrum is identical to that from spot #3 as modeled in Figure 9. (b) The spectrum is extracted from the location indicated by red star in Figure 4a.

outside the interbedded polyhydrated and monohydrated sulfate layers extends from the inside. However, the abundance similarity between the two kieserite units indicates that they might have formed at the same time during the same sedimentary process. The significant abundance difference between the two polyhydrated sulfate units may be due to differing amounts of Mg^{2+} and SO_4^{2-} ions in the two fluids from which the units precipitated. However, considering their spatial proximity, the solutions from which the sulfates were evaporated should have similar Mg^{2+} and SO_4^{2-} ion concentrations, assuming the depositional periods occurred at roughly similar times. Thus, a more likely scenario is that polyhydrated sulfates in the two units initially formed with similar abundances, and the polyhydrated sulfates in the interbedded unit 1 were subsequently partially dehydrated into kieserite, perhaps due to the presence of more complex brines with additional ions such as Cl^- [Wang et al., 2016]. Thus, the analysis of mineral abundances over the Melas Chasma sulfate deposits indicates that the formation of the interbedded polyhydrated and monohydrated sulfates is more consistent with the second hypothesis.

Jarosite has been found on the top of these hydrated sulfate deposits with ~12% volume abundance, intermixed with a significant amount of ferrihydrate with 28% volume abundance. On Mars, jarosite along with other sediments (e.g., Mg sulfates) could have formed by the evaporation of acid fluids that have interacted with and altered basaltic materials [Tosca et al., 2005]. To date, there have been no detailed reports of the identification of ferrihydrate on Mars, as this iron hydroxide does not have distinct absorption features in the VNIR wavelength region. In the Mawrth Vallis region, ferrihydrate was potentially identified based on a 1.93 μm absorption feature in the jarosite-bearing unit [Farrand et al., 2009], and the spectra with both 1.93 and 2.265 μm absorption bands were interpreted to be due to a mixture of jarosite and ferrihydrate. In Melas Chasma, jarosite has been unambiguously identified based on a 2.265 μm feature and the lack of water band at around 1.9 μm [Liu et al., 2012a]. Also, we found similar spectra as that found in Mawrth Vallis showing both 1.93 and 2.265 μm absorption bands. Our spectral unmixing modeling results, however, reveal that in the jarosite-bearing unit 1 (with no additional 1.93 μm band) there is still a certain amount of ferrihydrate present, whereas for the spectra with both the 1.93 and 2.265 μm absorption bands in the jarosite-bearing unit 2, the presence of ferrihydrate is not sufficient to reproduce the 1.93 μm feature and overall

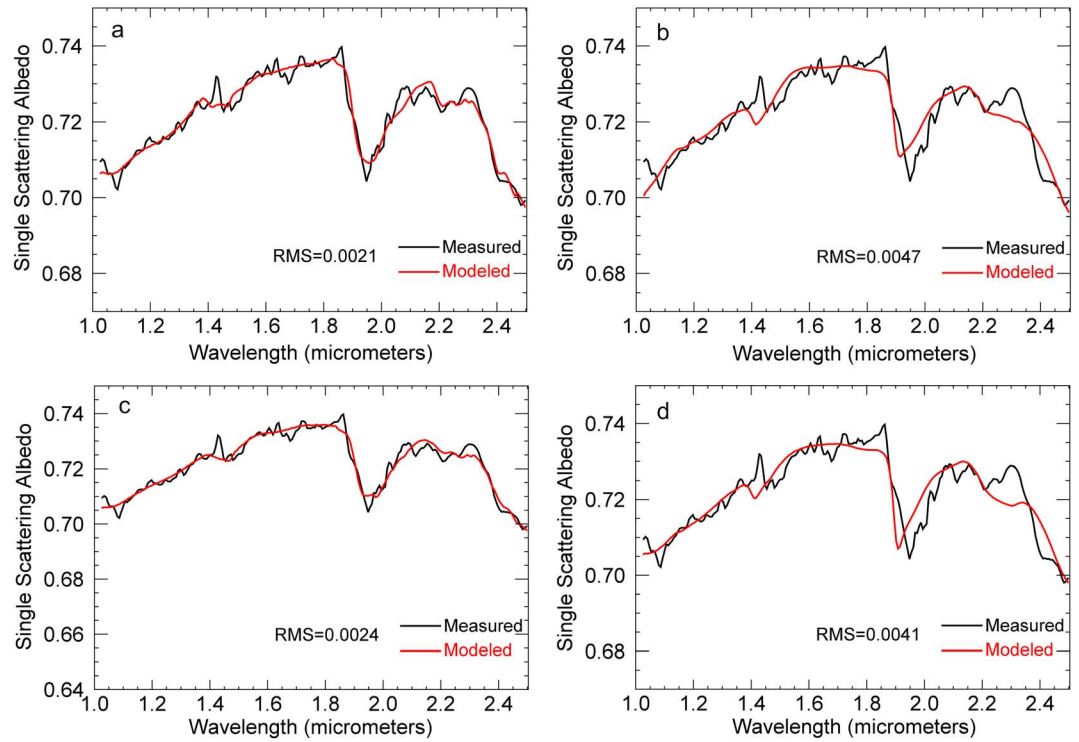


Figure 23. Grain size sensitivity test using the spectrum from spot #3 with polyhydrated sulfate signature. The constraints on the grain size for the spectral library end-members in the modeling are (a) fine-grained altered end-members and fine-grained primary end-members. (b) Coarse-grained altered end-members and coarse-grained primary end-members. (c) Fine-grained altered end-members and coarse-grained primary end-members. (d) Coarse-grained altered end-members and fine-grained primary end-members.

spectral shape. Instead, adding schwertmannite into the end-member library gives much better fit. Thus, our spectral unmixing gives further constraints on identification of mineral species. As an important set of minerals for understanding the past and present Martian environmental conditions, the ferric oxides, oxyhydroxides, and oxyhydroxysulfates including hematite, jarosite, ferrihydrite, goethite, and schwertmannite have been found at several locations on Mars [e.g., Christensen et al., 2000; Glotch and Christensen, 2005; Klingelhöfer et al., 2005; Bibring et al., 2006; Glotch and Rogers, 2007; Farrand et al., 2009; Liu et al., 2012b]. Of these ferric minerals, jarosite typically forms at pH values below 3, ferrihydrite forms at pH >3, schwertmannite precipitates at pH values between 2.8 and 4.5, and goethite forms throughout a range of pH from 2.5 to 8 [e.g., Bigham et al., 1996].

Schwertmannite has been predicted to be the major initial iron oxide precipitated from acidic sulfate-rich fluids interacting with an oxidizing environment [Hurowitz et al., 2010] and may form by itself or as an admixture with ferrihydrite [Raiswell et al., 2009, and references therein; Liu et al., 2012b]. Once formed, it may

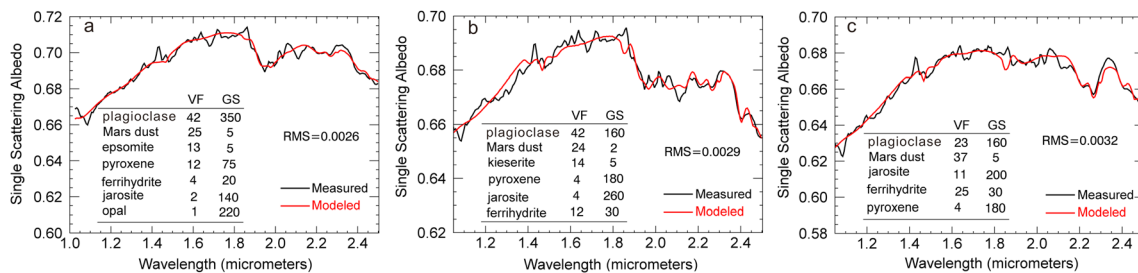


Figure 24. Example sensitivity testing results by excluding slope end-member in the unmixing model. (a) Derived mineral abundances and grain sizes for spot #1: Polyhydrated sulfates in the interbedded unit 1. (b) Derived mineral abundances and grain sizes for spot #4: Monohydrated sulfates outside the interbedded unit 1. (c) Derived mineral abundances and grain sizes for spot #5: Jarosite in the jarosite-bearing unit 1.

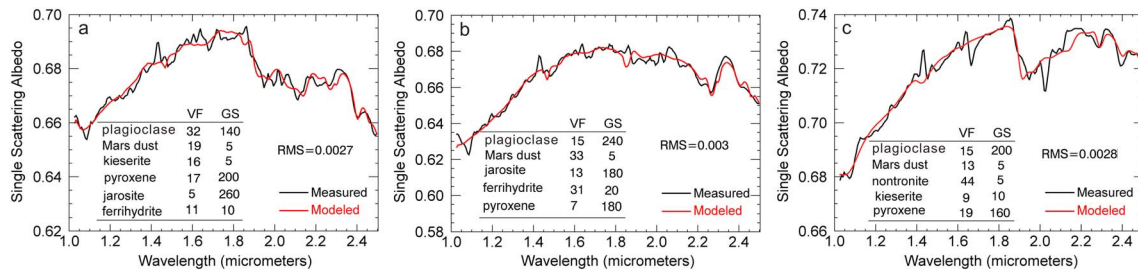


Figure 25. Example sensitivity testing results on plagioclase end-member by replacing the old spectrum with the new “cleaned” spectrum. The old spectrum has minor contamination from hydrated phases, and the new spectrum was obtained by manually modifying the optical constants to remove the absorption features due to hydrated phases. (a) Derived mineral abundances and grain sizes for spot #4: Monohydrated sulfates outside the interbedded unit 1. (b) Derived mineral abundances and grain sizes for spot #5: Jarosite in the jarosite-bearing unit 1. (c) Derived mineral abundances and grain sizes for spot #7: Phyllosilicates in the interbedded unit 2.

convert to a jarosite-goethite mixture under acidic pH conditions [Tosca *et al.*, 2008]. Note that goethite is not present based on our spectral unmixing analysis. In the acid mine drainage systems in southeast Pennsylvania, Cull *et al.* [2014] found natural precipitates of ferrihydrite, schwertmannite, and goethite, and the detailed spectroscopic analysis performed in their study indicates that ferrihydrite and schwertmannite may be masking goethite. Thus, the spectral masking effects on goethite may result in inaccurate descriptions of their abundances in spectral mixture models. Additional future laboratory work is required to address this issue.

Jarosite-bearing unit 2 contains substantial amounts of schwertmannite in addition to jarosite and ferrihydrite (~50% volume fraction in total) whereas jarosite-bearing unit 1 contains only jarosite and ferrihydrite also with a similar total volume fraction (~50%). Regardless of the presence of goethite in our study site, the jarosite and ferrihydrite assemblage in jarosite-bearing unit 1 could have formed through coprecipitation of jarosite-ferrihydrite-schwertmannite assemblage during the evaporation of an acidic fluid and transformation of schwertmannite into other phases upon changing aqueous conditions. As compared to jarosite-bearing unit 2, it is likely that the originally precipitated schwertmannite in jarosite-bearing unit 1 has all transformed into jarosite and/or ferrihydrite. Thus, knowing the exact assemblages and abundances is important, as the genetic link (coprecipitation and transformation) of these minerals can provide additional insight into the changing aqueous environments on Mars.

Another distinct feature that we observed in southwest Melas Chasma is the interbedded Fe/Mg smectites and sulfates (interbedded unit 2). As discussed in Liu and Catalano [2016], one possible formation mechanism is that the interbedded phyllosilicate-sulfate deposits formed through in situ basalt weathering and fluid evaporation, which also has been verified by geochemical modeling conducted in the same study. Alternatively, they may have formed through transport and deposition of detrital clay and subsequent evaporation. Understanding whether the phyllosilicates identified in the study area are detrital or authigenic is important, as different formation pathways lead to different hypothesized local environmental conditions. The coexistence of phyllosilicates and sulfates may record a temporal transition of aqueous history from alkaline to acidic conditions [Bibring *et al.*, 2006]. However, if the Fe/Mg smectites identified here are authigenic phyllosilicates, the Hesperian (or younger) aged Melas Chasma might have experienced environmental conditions that were conducive to the formation of phyllosilicates through in situ weathering and alteration, and thus, habitable conditions might have existed on Mars after the Noachian. Our spectral unmixing results show that Fe/Mg smectites are more prominent in the interbedded unit 2 with a ~40% volume abundance, whereas hydrated sulfates have an abundance of ~20%. Geochemical modeling performed in Liu and Catalano [2016] indicates that coupled basalt weathering and fluid evaporation can generate similar amounts

Table 3. Statistical Error of Model Abundance for the End-Members Listed in Section 4.2.1^a

End-Members	Spot 1_Epso	Spot 2_Kies	Spot 3_Epso	Spot 4_Kies	Spot 5_Jaro	Spot 6_Schw	Spot 9_Nont	Spot 7_Epso	Spot 8_Kies
Statistical error (%)	0.87	0.90	0.92	0.96	0.63	2.39	2.68	1.06	0.75

^aThe abbreviated names of minerals are Schw, schwertmannite; Epso, epsomite; Kies, kieserite; Jaro, jarosite; and Nont, nontronite.

of smectites and sulfate evaporites, which is not consistent with spectral unmixing results. However, the sulfate phases predicted to form during evaporation by modeling are all in polyhydrated states, whereas the observed sulfates contain both polyhydrated and monohydrated phases. Monohydrated sulfates could form through subsequent dehydration of polyhydrated sulfates [Wang *et al.*, 2016]. If a portion of the polyhydrated sulfates have dehydrated into kieserite, then the sulfate to phyllosilicate volume ratios predicted by thermodynamic calculations can be reduced to ~ 0.5 with the volume changes upon sulfate dehydration accounted, which is consistent with the volume abundance results derived by spectral unmixing models. Although an origin of detrital formation of phyllosilicates cannot entirely be excluded, the consistency between spectral unmixing results and thermodynamic modeling conducted previously indicates that the interbedded Fe/Mg smectites and sulfates more likely formed through coupled in situ basalt weathering and alteration and subsequent fluid evaporation.

7. Conclusions

In this study, we developed a full spectral unmixing analysis method to quantitatively study hydrated minerals in southwest Melas Chasma as observed by the CRISM instrument. A DISORT-based radiative transfer modeling approach was used to retrieve the single-scattering albedos from CRISM scenes, and the SSAs were then used to perform spectral mixture analysis. A variety of spectral end-members, including primary minerals, hydrated sulfates, phyllosilicates, iron oxyhydroxides, and Martian dust, were selected for our spectral library. Careful selection of spectral end-members for each targeted spectrum to be unmixed was performed using both visual inspection by comparing with laboratory spectra and the FATT end-member recovery technique. Mineral abundances were derived by spectral unmixing of the atmospherically corrected CRISM single-scattering albedos using the nonnegative least squares (NNLS) linear deconvolution algorithm. Spectral mixture modeling of the CRISM image cubes was performed to generate spatial distribution maps of mineral abundances that are used to compare with CRISM-derived index maps. The mineral abundance maps generated from spectral unmixing model agree well spatially with CRISM-derived parameter index maps, especially for the areas with high signal-to-noise ratios, although discrepancies exist between the two types of maps.

The initial mineral identifications using VNIR spectroscopy in southwest Melas Chasma provided clues to their alteration environments, and multiple formation mechanisms of these hydrated minerals have been hypothesized in the previous work [Liu and Glotch, 2014; Liu and Catalano, 2016]. However, the derived mineral abundances using our spectral unmixing technique performed in this work further constrain their formation. In the southern wall and nearby floor of Melas Chasma, the interbedded polyhydrated and monohydrated sulfates in the ILDs were interpreted to have formed either by cyclic evaporation and precipitation of the two hydrated sulfate phases from two episodic brines with different water chemistry, or through two precipitation-dehydration stages from a single complex Mg-Ca-Fe-SO₄-Cl brine. Our spectral mixture analysis results show that polyhydrated sulfates within the interbedded unit 1 have much lower abundances ($\sim 13\%$) than the surrounding polyhydrated sulfates (21%), which indicates that polyhydrated sulfates in the interbedded unit 1 might have been partially dehydrated into kieserite to form the interbedded strata and thus support the two-staged precipitation-dehydration formation hypothesis. In the jarosite-bearing unit 1, the spectral unmixing results show that there is $\sim 12\%$ jarosite intermixed with significant amount of ferrihydrite with $\sim 28\%$ volume abundance, whereas jarosite-bearing unit 2 contains substantial schwertmannite (34%) in addition to jarosite and ferrihydrite. The jarosite and ferrihydrite assemblage in jarosite-bearing unit 1 could have coprecipitated during the evaporation of an acidic fluid where the originally precipitated schwertmannite has entirely transformed into other phases upon changing aqueous conditions. It is unclear if goethite is also present due to the possible spectral masking effects from ferrihydrite and schwertmannite [Cull *et al.*, 2014]. Fe/Mg smectites are also identified in southwest Melas Chasma to be interbedded with hydrated sulfates. Our spectral unmixing results indicate that there are $\sim 40\%$ nontronite and $\sim 20\%$ hydrated sulfates in the interbedded strata. Together with the geochemical modeling results [Liu and Catalano, 2016], in situ coupled basalt weathering and evaporation may have initially produced similar amount of Fe/Mg smectites and polyhydrated sulfates, and the partial dehydration of polyhydrated sulfates into kieserite could have reduced the sulfate to phyllosilicate volume ratios to ~ 0.5 . The consistency between geochemical modeling and spectral unmixing results and the lack of evidence of the detrital origin of the phyllosilicates indicate that Fe/Mg smectites as observed in southwest Melas Chasma are likely authigenic clays.

The identification of interbedded polyhydrated and monohydrated sulfates, jarosite, and interbedded Fe/Mg smectites and sulfates in southwest Melas Chasma reveals a complex ancient aqueous history in this area. The spectral unmixing analysis method developed in this work provides mineral abundance information which gives additional constraints on their formation mechanism. The results have shed additional insight on the aqueous history of the study area. Our analyses suggest that a comprehensive understanding of the formation conditions of the hydrated minerals requires multiple investigation techniques, which include but are not limited to, initial mineral phase identifications using remote sensed data, laboratory studies, geochemical modeling, spectral unmixing analysis, and even in situ investigation by robotic missions.

Acknowledgments

We would like to thank Marion Massé and two anonymous reviewers for their constructive comments that significantly improved the content and clarity of the manuscript. We are very grateful for the excellent work of the NASA MRO project team and the CRISM Science Operations Center (SOC). All orbital data sets used in this study are available at the Mars Orbital Data Explorer of the Washington University in Saint Louis (<http://ode.rsl.wustl.edu/mars/>).

References

- Adams, J. B., M. O. Smith, and P. E. Johnson (1986), Spectral mixture modeling—A new analysis of rock and soil types at the Viking Lander-1 site, *J. Geophys. Res.*, *91*, 8098–8112, doi:10.1029/JB091iB08p08098.
- Adams, J. B., M. O. Smith, and A. R. Gillespie (1993), *Remote Geochemical Analysis: Elemental and Mineralogical Composition*, pp. 145–166, Cambridge Univ. Press, New York.
- Arvidson, R. E., F. Poulet, J.-P. Bibring, M. J. Wolff, A. Gendrin, R. V. Morris, J. J. Freeman, Y. Langevin, N. Mangold, and G. Bellucci (2005), Spectral reflectance and morphologic correlations in eastern Terra Meridiani, Mars, *Science*, *307*, 1591–1594, doi:10.1126/science.1109509.
- Arvidson, R. E., et al. (2006), Nature and origin of the hematite-bearing plains of Terra Meridiani based on analyses of orbital and Mars Exploration rover data sets, *J. Geophys. Res.*, *111*, E12S08, doi:10.1029/2006JE002728.
- Atkinson, P. M., M. E. J. Cutler, and H. Lewis (1997), Mapping sub-pixel proportional land cover with AVHRR imagery, *Int. J. Remote Sens.*, *18*, 917–935.
- Bandfield, J. L., P. R. Christensen, and M. D. Smith (2000), Spectral data set factor analysis and end-member recovery: Application to analysis of Martian atmospheric particulates, *J. Geophys. Res.*, *105*(E4), 9573–9587, doi:10.1029/1999JE001094.
- Bibring, J.-P., et al. (2004), OMEGA: Observatoire pour la Minéralogie, l'Eau, les Glaces et l'Activité, in *Mars Express: The Scientific Payload*, Eur. Space Agency Spec. Publ., ESA-1240, edited by A. Wilson, pp. 37–49.
- Bibring, J.-P., et al. (2005), Mars surface diversity as revealed by the OMEGA/Mars Express observations, *Science*, *307*(5715), 1576–1581, doi:10.1126/science.1109509.
- Bibring, J.-P., et al. (2006), Global mineralogical and aqueous Mars history derived from OMEGA/Mars Express data, *Science*, *312*(5772), 400–404, doi:10.1126/science.1122659.
- Bigham, J. M., U. Schwertmann, and G. Pfab (1996), Influence of pH on mineral speciation in a bioreactor simulating acid mine drainage, *Appl. Geochem.*, *11*, 845–849, doi:10.1016/S0883-2927(96)00052-2.
- Borel, C. C., and S. A. Gerstl (1994), Nonlinear spectral mixing models for vegetative and soil surface, *Remote Sens. Environ.*, *47*, 403–416.
- Cahill, J. T. S., P. G. Lucey, and M. A. Wiczorek (2009), Compositional variations of the lunar crust: Results from radiative transfer modeling of central peak spectra, *J. Geophys. Res.*, *114*, E09001, doi:10.1092/2008JE003282.
- Carpenter, G. A., S. Gopal, S. Macomber, S. Martens, and C. E. Woodstock (1999), A neural network method for mixture estimation for vegetation mapping, *Remote Sens. Environ.*, *70*, 138–152.
- Catalano, J. G., A. R. Beehr, and R. E. Arvidson (2012), Thermodynamic and mass balance constraints on phyllosilicate and evaporite formation scenarios on early Mars, in *Third Conference on Early Mars*, Abstract 7010, Lake Tahoe, Nevada, 21–25 May.
- Che, C., and T. D. Glotch (2014), Thermal alteration: A possible reason for the inconsistency between OMEGA/CRISM and TES detections of phyllosilicates on Mars? *Geophys. Res. Lett.*, *41*, 321–327, doi:10.1002/2013GL058649.
- Christensen, P. R., et al. (2000), Detection of crystalline hematite mineralization on Mars by the Thermal Emission Spectrometer: Evidence for near-surface water, *J. Geophys. Res.*, *105*, 9623–9642, doi:10.1029/1999JE001093.
- Clark, B. E. (1995), Spectral mixing models of S-type asteroids, *J. Geophys. Res.*, *100*, 14,443–14,456, doi:10.1029/95JE00720.
- Clark, B. E., et al. (2001), Space weathering on Eros: Constraints from albedo and spectral measurements of Psyche crater, *Meteorit. Planet. Sci.*, *36*, 1617–1637.
- Clark, R. N. (1983), Spectral properties of mixtures of montmorillonite and dark carbon grains: Implications for remote sensing minerals containing chemically and physically adsorbed water, *J. Geophys. Res.*, *88*, 10,635–10,644, doi:10.1029/JB088iB12p10635.
- Clark, R. N., and T. L. Roush (1984), Reflectance spectroscopy: Quantitative analysis techniques for remote sensing applications, *J. Geophys. Res.*, *89*, 6329–6340, doi:10.1029/JB089iB07p06329.
- Clark, R. N., T. V. V. King, M. Klejwa, G. A. Swayze, and N. Vergo (1990), High spectral resolution reflectance spectroscopy of minerals, *J. Geophys. Res.*, *95*, 12,653–12,680, doi:10.1029/JB095iB08p12653.
- Cloutis, E. A., et al. (2006), Detection and discrimination of sulfate minerals using reflectance spectroscopy, *Icarus*, *184*, 121–157, doi:10.1016/j.icarus.2006.04.003.
- Combe, J.-P., et al. (2008), Analysis of OMEGA/Mars Express data hyperspectral data using a Multiple-Endmember Linear Spectral Unmixing Model (MELSUM): Methodology and first results, *Planet. Space Sci.*, *56*, 951–975.
- Cull, S., R. E. Arvidson, M. Mellon, S. Wiseman, R. Clark, T. Titus, R. V. Morris, and P. McGuire (2010a), Seasonal H₂O and CO₂ ice cycles at the Mars Phoenix landing site: 1. Prelanding CRISM and HiRISE observations, *J. Geophys. Res.*, *115*, E00D16, doi:10.1029/2009JE003340.
- Cull, S., R. E. Arvidson, R. V. Morris, M. Wolff, M. T. Mellon, and M. T. Lemmon (2010b), Seasonal ice cycle at the Mars Phoenix landing site: 2. Postlanding CRISM and ground observations, *J. Geophys. Res.*, *115*, E00E19, doi:10.1029/2009JE003410.
- Cull, S., C. A. Cravotta III, J. G. Klings, and C. Weeks (2014), Spectral masking of goethite in abandoned mine drainage systems: Implications for Mars, *Earth Planet. Sci. Lett.*, *403*, 217–224, doi:10.1016/j.epsl.2014.06.045.
- Denevi, B. W., P. G. Lucey, and S. B. Sherman (2008), Radiative transfer modeling of near infrared spectra of lunar mare soils: Theory and measurement, *J. Geophys. Res.*, *113*, E02003, doi:10.1029/2007JE002929.
- Edgett, K. S., and P. R. Christensen (1991), The particle size of Martian aeolian dunes, *J. Geophys. Res.*, *96*(E5), 22,765–22,776, doi:10.1029/91JE02412.
- Edwards, C. S., and B. L. Ehlmann (2015), Carbon sequestration on Mars, *Geology*, *43*(10), 863–866, doi:10.1130/G36983.1.
- Ehlmann, B. L., et al. (2009), Identification of hydrated silicate minerals on Mars using MRO-CRISM: Geologic context near Nili Fossae and implications for aqueous alteration, *J. Geophys. Res.*, *114*, E00D08, doi:10.1029/2009JE003339.

- Ehlmann, B. L., G. Berger, N. Mangold, J. R. Michalski, D. C. Catling, S. W. Ruff, E. Chassefière, P. B. Niles, V. Chevrier, and F. Poulet (2013), Geochemical consequences of widespread clay mineral formation in Mars' ancient crust, *Space Sci. Rev.*, *174*, 329–364, doi:10.1007/s11214-012-9930-0.
- Farrand, W. H., T. D. Glotch, J. W. Rice Jr., J. A. Hurowitz, and G. A. Swayze (2009), Discovery of jarosite within the Mawrth Vallis region of Mars: Implications for the geologic history of the region, *Icarus*, *204*, 478–488, doi:10.1016/j.icarus.2009.07.014.
- Friedlander, L. R., T. D. Glotch, D. L. Bish, M. D. Dyar, T. G. Sharp, E. C. Sklute, and J. R. Michalski (2015), Structural and spectroscopic changes to natural nontronite induced by experimental impacts between 10 and 40 GPa, *J. Geophys. Res. Planets*, *120*, 888–912, doi:10.1002/2014JE004638.
- Gendrin, A., et al. (2005), Sulfates in Martian layered terrains: The OMEGA/Mars Express view, *Science*, *307*, 1587–1591, doi:10.1126/science.1109087.
- Glotch, T. D., and P. R. Christensen (2005), Geologic and mineralogic mapping of Aram Chaos: Evidence for a water-rich history, *J. Geophys. Res.*, *110*, E09006, doi:10.1029/2004JE002389.
- Glotch, T. D., and A. D. Rogers (2007), Aqueous deposition of hematite and sulfate-rich light-toned layered deposits in Aureum and Iani Chaos, Mars, *J. Geophys. Res.*, *112*, E06001, doi:10.1029/2006JE00286.
- Glotch, T. D., and A. D. Rogers (2013), Evidence for magma-carbonate interaction beneath Syrtis Major, Mars, *J. Geophys. Res. Planets*, *118*, 126–137, doi:10.1029/2012JE004230.
- Glotch, T. D., J. L. Bandfield, P. R. Christensen, W. M. Calvin, S. M. McLennan, B. C. Clark, A. D. Rogers, and S. W. Squyres (2006), The mineralogy of the light-toned outcrop at Meridiani Planum as seen by the Miniature Thermal Emission Spectrometer and implications for its formation, *J. Geophys. Res.*, *111*, E12S03, doi:10.1029/2005JE002672.
- Goudge, T. A., J. F. Mustard, J. W. Head, M. R. Salvatore, and S. M. Wiseman (2015), Integrating CRISM and TES hyperspectral data to characterize a halloysite-bearing deposit in Kashira crater, Mars, *Icarus*, *250*, 165–187, doi:10.1016/j.icarus.2014.11.034.
- Guilfoyle, K. J., M. L. Althouse, and C. I. Chang (2001), A quantitative and comparative analysis of linear and nonlinear spectral mixture models using radial basis function neural networks, *IEEE Trans. Geosci. Remote Sens.*, *39*, 2314–2318.
- Hapke, B. (1981), Bidirectional reflectance spectroscopy: 1. Theory, *J. Geophys. Res.*, *86*(B4), 3039–3054, doi:10.1029/JB086iB04p03039.
- Hapke, B. (1993), *Theory of Reflectance and Emittance Spectroscopy*, Cambridge Univ. Press, Cambridge, U. K.
- Hapke, B., and E. Wells (1981), Bidirectional reflectance spectroscopy: 2. Experiments and observations, *J. Geophys. Res.*, *86*, 3055–3060, doi:10.1029/JB086iB04p03055.
- Hiroi, T., and C. M. Pieters (1994), Estimation of grain sizes and mixing ratios of fine powder mixtures of common geologic minerals, *J. Geophys. Res.*, *99*, 10,867–10,879, doi:10.1029/94JE00841.
- Hurowitz, J. A., W. W. Fischer, N. J. Tosca, and R. E. Milliken (2010), Origin of acidic surface waters and the evolution of atmospheric chemistry on early Mars, *Nat. Geosci.*, *3*, 323–326, doi:10.1038/ngeo831.
- Johnson, P. E., M. O. Smith, and J. B. Adams (1992), Simple algorithms for remote determination of mineral abundances and particles size from reflectance spectra, *J. Geophys. Res.*, *97*, 2649–2657, doi:10.1029/91JE02504.
- Keshava, N., and J. F. Mustard (2002), Spectral unmixing, *IEEE Signal Process. Mag.*, *19*(1), 44–57.
- Klingelhöfer, G., E. DeGrave, R. V. Morris, A. Van Alboom, V. G. de Resende, P. A. De Souza, and D. Rodinov (2005), Mössbauer spectroscopy of Mars: Goethite in the Columbia Hills at Gusev Crater, *Hyperfine Interact.*, *166*, 549–554, doi:10.1007/978-3-540-49850-6_86.
- Langevin, Y., F. Poulet, J.-P. Bibring, and B. Gondet (2005), Sulfates in the north polar region of Mars detected by OMEGA/Mars Express, *Science*, *307*, 1584–1586, doi:10.1126/science.1109091.
- Lawrence, S. J., and P. G. Lucey (2007), Radiative transfer models of meteoritic assemblages, *J. Geophys. Res.*, *112*, E07005, doi:10.1029/2006JE002765.
- Li, L., and J. F. Mustard (2003), Highland contamination in lunar mare soils: Improved mapping with multiple end-member spectral mixture analysis (MESMA), *J. Geophys. Res.*, *108*(E6), 5053, doi:10.1029/2002JE001917.
- Liu, Y., and J. G. Catalano (2016), Implications for the aqueous history of southwest Melas Chasma as revealed by interbedded hydrated sulfates and Fe/Mg smectites, *Icarus*, *271*, 283–291, doi:10.1016/j.icarus.2016.02.015.
- Liu, Y., and T. D. Glotch (2014), Implication on aqueous history of Mars as revealed by hydrous minerals in southwest Melas Chasma, Abstract 1438 for Eighth International Conference on Mars, Pasadena, Los Angeles, Calif.
- Liu, Y., R. E. Arvidson, R. Li, and W. Wang (2012a), Hydrated minerals associated with interior layered deposits near the southern wall of Melas Chasma, Valles Marineris, Mars Abstract 2572 for 43rd Lunar and Planetary Science Conference, The Woodlands, Tex.
- Liu, Y., R. E. Arvidson, M. J. Wolff, M. T. Mellon, J. G. Catalano, A. Wang, and J. L. Bishop (2012b), Lambert albedo retrieval and analyses over Aram Chaos from OMEGA hyperspectral imaging data, *J. Geophys. Res.*, *117*, E00J11, doi:10.1029/2012JE004056.
- Lucey, P. G. (1998), Model near-infrared optical constants of olivine and pyroxene as a function of iron content, *J. Geophys. Res.*, *103*(E1), 1703–1713, doi:10.1029/97JE03145.
- Lucey, P. G., and S. K. Noble (2008), Experimental test of a radiative transfer model of the optical effects of space weathering, *Icarus*, *197*, 348–353.
- Malinowski, E. R. (1991), *Factor Analysis in Chemistry*, 2nd ed., Wiley-Interscience, New York.
- Mangold, N., C. Quantin, V. Ansan, C. Delacourt, and P. Allemand (2004), Evidence for precipitation on Mars from dendritic valleys in the Valles Marineris area, *Science*, *305*(5680), 78–81, doi:10.1126/science.1097549.
- Martone, A. A., and T. D. Glotch (2014), The effect of grain size and abundance on the deconvolution of mixtures using the Shkuratov model, *Lunar Planet. Sci. XLV*, Abstract 2295.
- Metz, J., J. Grotzinger, C. Okubo, and R. Milliken (2010), Thin-skinned deformation of sedimentary rocks in Valles Marineris, Mars, *J. Geophys. Res.*, *115*, E11004, doi:10.1029/2010JE003593.
- Milliken, R., et al. (2008), Opaline silica in young deposits on Mars, *Geology*, *36*, 847–850, doi:10.1130/G24967A.1.
- Murchie, S., et al. (2007), Compact Reconnaissance Imaging Spectrometer for Mars (CRISM) on Mars Reconnaissance Orbiter (MRO), *J. Geophys. Res.*, *112*, E05S03, doi:10.1029/2006JE002682.
- Murchie, S. L., et al. (2009a), A synthesis of Martian aqueous mineralogy after 1 Mars year of observations from the Mars Reconnaissance Orbiter, *J. Geophys. Res.*, *114*, E00D06, doi:10.1029/2009JE003342.
- Murchie, S. L., et al. (2009b), Compact Reconnaissance Imaging Spectrometer for Mars investigation and data set from the Mars Reconnaissance Orbiter's primary science phase, *J. Geophys. Res.*, *114*, E00D07, doi:10.1029/2009JE003344.
- Mustard, J. F., and C. M. Pieters (1989), Photometric phase functions of common geologic minerals and applications to quantitative analysis of mineral mixture reflectance spectra, *J. Geophys. Res.*, *94*, 13,619–13,634, doi:10.1029/JB094iB10p13619.
- Mustard, J. F., L. Li, and G. He (1998), Nonlinear spectral mixture modeling of lunar multispectral data: Implications for lateral transport, *J. Geophys. Res.*, *103*, 19,419–19,425, doi:10.1029/98JE01901.
- Mustard, J. F., et al. (2008), Hydrated silicate minerals on Mars observed by the Mars Reconnaissance Orbiter CRISM instrument, *Nature*, *454*, 305–309, doi:10.1038/nature07097.

- Nash, D. B., and J. E. Conel (1974), Spectral reflectance systematics for mixtures of powdered hypersthene, labradorite, and ilmenite, *J. Geophys. Res.*, *79*, 1615–1621, doi:10.1029/JB079i011p01615.
- Poulet, F., and S. Erard (2004), Nonlinear spectral mixing: Quantitative analysis of laboratory mineral mixtures, *J. Geophys. Res.*, *109*, E02009, doi:10.1029/2003JE002179.
- Poulet, F., J. N. Cuzzi, D. P. Cruikshank, T. Roush, and C. M. Dalle Ore (2002), Comparison between the Shkuratov and Hapke scattering theories for solid planetary surfaces: Application to the surface composition of two Centaurs, *Icarus*, *160*, 313–324.
- Poulet, F., J.-P. Bibring, J. F. Mustard, A. Gendrin, N. Mangold, Y. Langevin, R. E. Arvidson, B. Gondet, and C. Gomez (2005), Phyllosilicates on Mars and implications for early Martian climate, *Nature*, *438*, 623–627, doi:10.1038/nature04274.
- Poulet, F., N. Mangold, D. Loizeau, J.-P. Bibring, Y. Langevin, J. Michalski, and B. Gondet (2008), Abundance of minerals in the phyllosilicate-rich units on Mars, *Astron. Astrophys.*, *487*, L41–L44, doi:10.1051/0004-6361:200810150.
- Poulet, F., J.-P. Bibring, Y. Langevin, J. F. Mustard, N. Mangold, M. Vincendon, B. Gondet, P. Pinet, J.-M. Bardintzeff, and B. Platevoet (2009), Quantitative compositional analysis of Martian mafic regions using MEX/OMEGA reflectance data: 1. Methodology, uncertainties and examples of application, *Icarus*, *201*, 69–83.
- Poulet, F., J. Carter, J. L. Bishop, D. Loizeau, and S. M. Murchie (2014), Mineral abundances at the final four curiosity study sites and implications for their formation, *Icarus*, *231*, 65–76, doi:10.1016/j.icarus.2013.11.023.
- Putzig, N. E., and M. T. Mellon (2007), Apparent thermal inertia and the surface heterogeneity of Mars, *Icarus*, *191*, 68–94, doi:10.1016/j.icarus.2007.05.013.
- Quantin, C., P. Allemand, N. Mangold, G. Dromart, and C. Delacourt (2005), Fluvial and lacustrine activity on layered deposits in Melas Chasma, Valles Marineris, Mars, *J. Geophys. Res.*, *110*, E12S19, doi:10.1029/2005JE002440.
- Raiswell, R., L. G. Benning, L. Davidson, M. Tranter, and S. Tulaczyk (2009), Schwertmannite in wet, acid, and oxic microenvironments beneath polar and polythermal glaciers, *Geology*, *37*, 431–434, doi:10.1130/G25350A.1.
- Ramsey, M. S., and P. R. Christensen (1998), Mineral abundance determination: Quantitative deconvolution of thermal emission spectra, *J. Geophys. Res.*, *103*(B1), 577–596, doi:10.1029/97JB02784.
- Roberts, D. A., S. L. Ustin, S. Ogunjemiyo, J. Greenberg, S. Z. Dobrowski, and J. Q. Chen (2004), Spectral and structural measures of northwest forest vegetation at leaf to landscape scales, *Ecosystems*, *7*, 545–562.
- Robertson, K. M., R. E. Milliken, and S. Li (2016), Estimating mineral abundances of clay and gypsum mixtures using radiative transfer models applied to visible-near infrared reflectance spectra, *Icarus*, *277*, 171–186, doi:10.1016/j.icarus.2016.04.034.
- Rogers, A. D., and O. Aharonson (2008), Mineralogical composition of sands in Meridiani Planum determined from MER data and comparison to orbital measurements, *J. Geophys. Res.*, *E06S14*, doi:10.1029/2007JE002995.
- Scudder, N. A., T. D. Glotch, Y. Liu, and T. Condu (2015), Hapke-based linear spectral unmixing of CRISM single scattering albedo data Lunar Planet. Sci., XLV, Abstract 2977.
- Shaw, A., M. J. Wolff, F. P. Seelos, S. M. Wiseman, and S. Cull (2013), Surface scattering properties at the Opportunity Mars rover's traverse region measured by CRISM, *J. Geophys. Res. Planets*, *118*, 1699–1717, doi:10.1002/jgre.20119.
- Shkuratov, Y. G., L. Starukhina, H. Hoffmann, and G. Arnold (1999), A model of spectral albedo of particulate surfaces: Implications for optical properties of the Moon, *Icarus*, *137*, 235–246.
- Singer, R. B. (1981), Near-infrared spectral reflectance of mineral mixtures: Systematic combinations of pyroxenes, olivine, and iron oxides, *J. Geophys. Res.*, *86*, 7967–7982, doi:10.1029/JB086iB09p07967.
- Sklute, E. C., T. D. Glotch, J. Piatek, W. Woerner, A. Martone, and M. Kraner (2015), Optical constants of synthetic potassium, sodium, and hydronium jarosite, *Am. Mineral.*, *100*, 1110–1122.
- Smith, M. D., M. J. Wolff, R. T. Clancy, and S. L. Murchie (2009), Compact Reconnaissance Imaging Spectrometer observations of water vapor and carbon monoxide, *J. Geophys. Res.*, *114*, E00D03, doi:10.1029/2008JE003288.
- Somers, B., G. P. Asner, L. Tits, and P. Coppin (2011), Endmember variability in spectral mixture analysis: A review, *Remote Sens. Environ.*, *115*, 1603–1616.
- Stamnes, K., S. Tsay, W. Wiscombe, and K. Jayaweera (1988), Numerically stable algorithm for discrete-ordinate-method radiative transfer in multiple scattering and emitting layered media, *Appl. Opt.*, *27*, 2502–2509.
- Thomson, J. L., and J. W. Salisbury (1993), The mid-infrared reflectance at mineral mixtures (7–14 μm), *Remote Sens. Environment*, *45*, 1–13.
- Thomas, N. H., and J. L. Bandfield (2013), Identification of spectral endmembers in CRISM data using factor analysis and target transformation Lunar Planet. Sci. XLIV, Abstract 1325.
- Tosca, N. J., S. M. McLennan, B. C. Clark, J. P. Grotzinger, J. A. Hurowitz, A. H. Knoll, C. Schröder, and S. W. Squyres (2005), Geochemical modeling of evaporation processes on Mars: Insight from the sedimentary record at Meridiani Planum, *Earth Planet. Sci. Lett.*, *240*, 122–148, doi:10.1016/j.epsl.2005.09.042.
- Tosca, N. J., S. M. McLennan, M. D. Dyar, E. C. Sklute, and F. M. Michel (2008), Fe oxidation processes at Meridiani Planum and implications for secondary Fe mineralogy on Mars, *J. Geophys. Res.*, *113*, E05005, doi:10.1029/2007JE003019.
- Viviano-Beck, C. E., et al. (2014), Revised CRISM spectral parameters and summary products based on the currently detected mineral diversity on Mars, *J. Geophys. Res. Planets*, *119*, 1403–1431, doi:10.1002/2014JE004627.
- Wang, A., B. L. Jolliff, Y. Liu, and K. Connor (2016), Setting constraints on the nature and origin of the two major hydrous sulfates on Mars: Monohydrated and polyhydrated sulfates, *J. Geophys. Res. Planets*, *121*, 678–694, doi:10.1002/2015JE004889.
- Weitz, C. M., T. J. Parker, M. H. Bulmer, F. Scott Anderson, and J. A. Grant (2003), Geology of the Melas Chasma landing site for the Mars Exploration Rover mission, *J. Geophys. Res.*, *108*(E12), 8082, doi:10.1029/2002JE002022.
- Weitz, C. M., E. Noe Dobrea, and J. J. Wray (2015), Mixtures of clays and sulfates within deposits in western Melas Chasma, *Icarus*, *252*, 291–314, doi:10.1016/j.icarus.2014.04.009.
- Wiseman, S. M., et al. (2014), Characterization of artifacts introduced by the empirical volcano-scan atmospheric correction commonly applied to CRISM and OMEGA near-infrared spectra, *Icarus*, *269*, 11–121, doi:10.1016/j.icarus.2014.10.012.
- Wolff, M. J., R. T. Clancy, M. D. Smith, CRISM Science Team, and Marci Science Team (2007), Some studies of Martian aerosol properties using MRO/CRISM and MRO/Marci, in *Seventh International Conference on Mars, LPI Contrib.*, vol. 1353, pp. 3121, CD-ROM, Pasadena, Calif.
- Wolff, M. J., M. D. Smith, R. T. Clancy, R. E. Arvidson, M. Kahre, F. P. Seelos IV, S. L. Murchie, H. Savijärvi, and the CRISM Science Team (2009), Wavelength dependence of dust aerosol single scattering albedo as observed by CRISM, *J. Geophys. Res.*, *114*, E00D04, doi:10.1029/2009JE003350.